Available online at www.sciencedirect.com
SCIENCE DIRECT®
Tectonophysics 371 (2003) 81–110
TECTONOPHYSICS
www.elsevier.com/locate/tecto

"DOBREfraction'99"—velocity model of the crust and upper mantle beneath the Donbas Foldbelt (East Ukraine)

The DOBREfraction'99 Working Group
M. Grad[a], D. Gryn[b], A. Guterch[c], T. Janik[c], R. Keller[d], R. Lang[e], S.B. Lyngsie[e], V. Omelchenko[b], V.I. Starostenko[b], R.A. Stephenson[f,*], S.M. Stovba[g], H. Thybo[e], A. Tolkunov[g]

[a] *Institute of Geophysics, University of Warsaw, Pasteura 7, 02-093 Warsaw, Poland*
[b] *Institute of Geophysics, National Academy of Sciences of Ukraine, Palladin av. 32, 252680 Kyiv, Ukraine*
[c] *Institute of Geophysics, Polish Academy of Sciences, Ks. Janusza 64, 01-452 Warsaw, Poland*
[d] *Department of Earth Sciences, University of Texas at El Paso, El Paso, TX, USA*
[e] *Geological Institute, University of Copenhagen, Øster Voldgade 10, DK-1350 Copenhagen K, Denmark*
[f] *Department of Tectonics and Structural Geology, Faculty of Earth and Life Sciences, Vrije Universiteit, De Boelelaan 1085, 1081 HV Amsterdam, Netherlands*
[g] *Ukrgeofisika, Technology Centre, Sophia Perovska 10, 03057 Kyiv, Ukraine*

Received 25 July 2002; accepted 25 April 2003

Abstract

The Donbas Foldbelt (DF) is the uplifted and deformed part of the up to 20-km-thick Dniepr–Donets Basin (DDB) that formed as the result of rifting of the East European Craton (EEC) in the Late Devonian. Uplift, especially of the southern margin of the basin, occurred in Early Permian times, in a (trans)tensional tectonic stress regime while folding and reverse faulting mainly occurred later—mainly during the Late Cretaceous. A seismic refraction/wide-angle reflection survey was carried out in 1999 (DOBREfraction'99) to complement existing Deep Seismic Sounding (DSS) data from the area that did not record significant Pn phase arrivals because of insufficient maximum offset. DOBREfraction'99 comprised some 245 recording stations along a line of 360 km length with 11 in-line shot points as well as a 100 km away, parallel 190 km long subsidiary fan profile. The main profile runs between the shores of the Azov Sea in the south to the Ukraine–Russia border in the north, across the Azov Massif (Ukrainian Shield), the Foldbelt, and the Voronezh Massif. Particular scientific targets include the nature of the crust–mantle transition and the geometry of crustal–upper mantle structures related to rifting and subsequent basin inversion. Tomographic inversion as well as ray-trace based velocity modelling has been carried out. The velocity signature of the sedimentary basin itself is well resolved, indicating an asymmetric form, with a steeper basement surface in the south than in the north, and a total thickness of about 20 km. A thick (>10 km) high velocity (>6.9 km/s) lower crustal body lies beneath the rift basin itself, offset slightly to the north compared to the main basin depocentre, likely related to the rifting processes. Velocities in the crust below the Ukrainian Shield, south of the

* Corresponding author. Authors' names are listed alphabetically.
E-mail address: randell.stephenson@falw.vu.nl (R.A. Stephenson).

doi:10.1016/S0040-1951(03)00211-7

Foldbelt, are in general higher than beneath the Voronezh Massif to the north. The Moho displays only slight topography around a depth of 40 km along the profile.

Keywords: Dniepr–Donets Basin; Donbas Foldbelt; Intraplate deformation; Intracratonic rifting; Seismic refraction; Crustal and upper mantle structure

1. Introduction

The Dniepr–Donets Basin (DDB) is a Late Devonian rift basin located on the southwestern part of the East European Craton (EEC), striking in a southeasterly direction to the contiguous Donbas Foldbelt (DF) in eastern Ukraine and in southern Russia where it joins the deformed southern margin of the EEC (Karpinsky Swell). The width of the rift (shaded in Fig. 1) varies between 60 and 70 km in the northwest and 140–160 km in the southeast. Sediment thicknesses (comprising Late Devonian syn-rift and Carboniferous–Palaeogene post-rift successions) increase from about 2 km in the northwest to about 20 km in

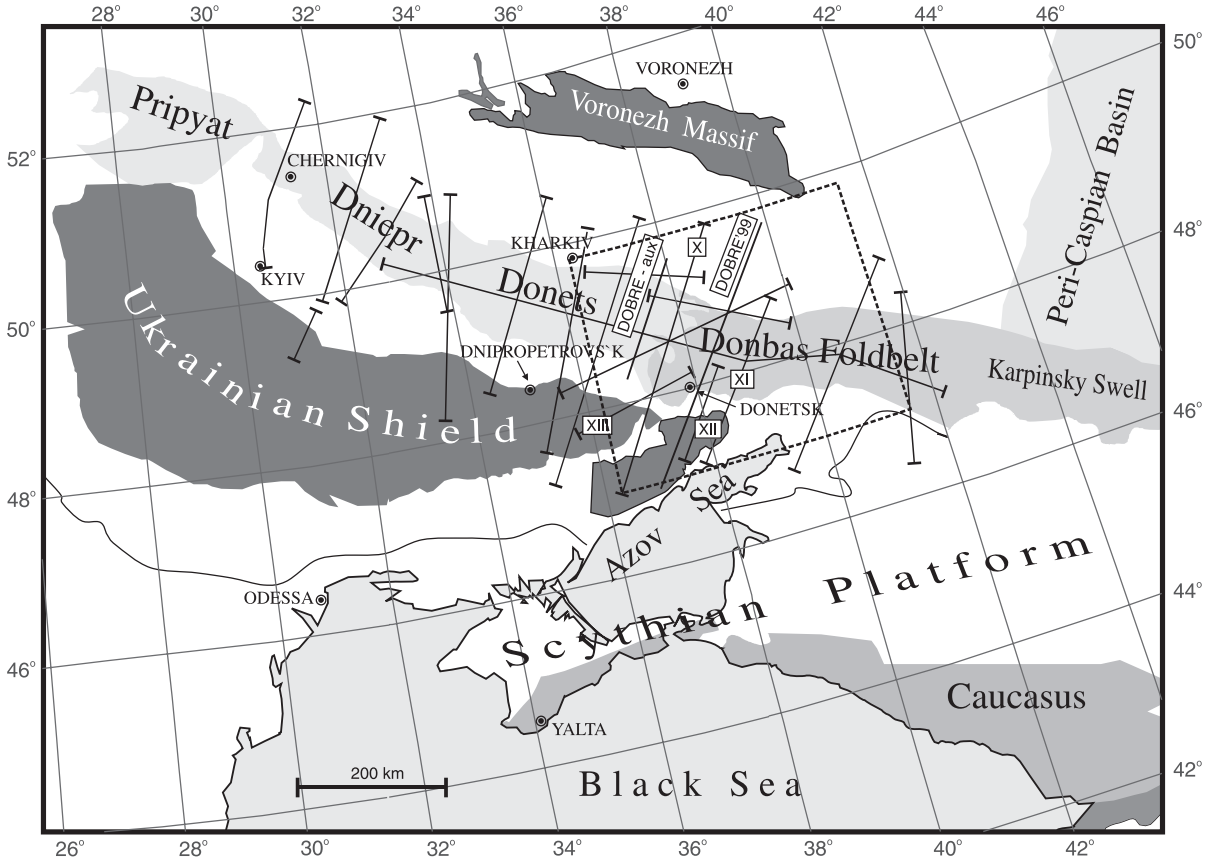

Fig. 1. Regional tectonic setting of the Dniepr–Donets Basin and its contiguous, inverted, segment, the Donbas Foldbelt (lightly shaded within the inferred boundaries of the original Devonian rift basin), lying between the Precambrian Ukrainian Shield and Voronezh Massif (darker shading). Ornamented lines in the vicinity of the rift represent DSS profiles crossing the Dniepr–Donets Basin that existed prior to acquisition of DOBREfraction'99; profiles labelled X–XIII are mentioned in the text. The dashed line box indicates the outline of the map shown in Fig. 2.

the Donets segment of the basin (e.g. Stephenson et al., 2001). Devonian rifting was accompanied by major magmatic activity and the uplift of the Ukrainian Shield and the Voronezh Massif, forming a large radius arch that is transected by the DDB (e.g. Stephenson et al., 2001).

There are profound along strike variations in the degree of basin "inversion" in the DDB, ranging

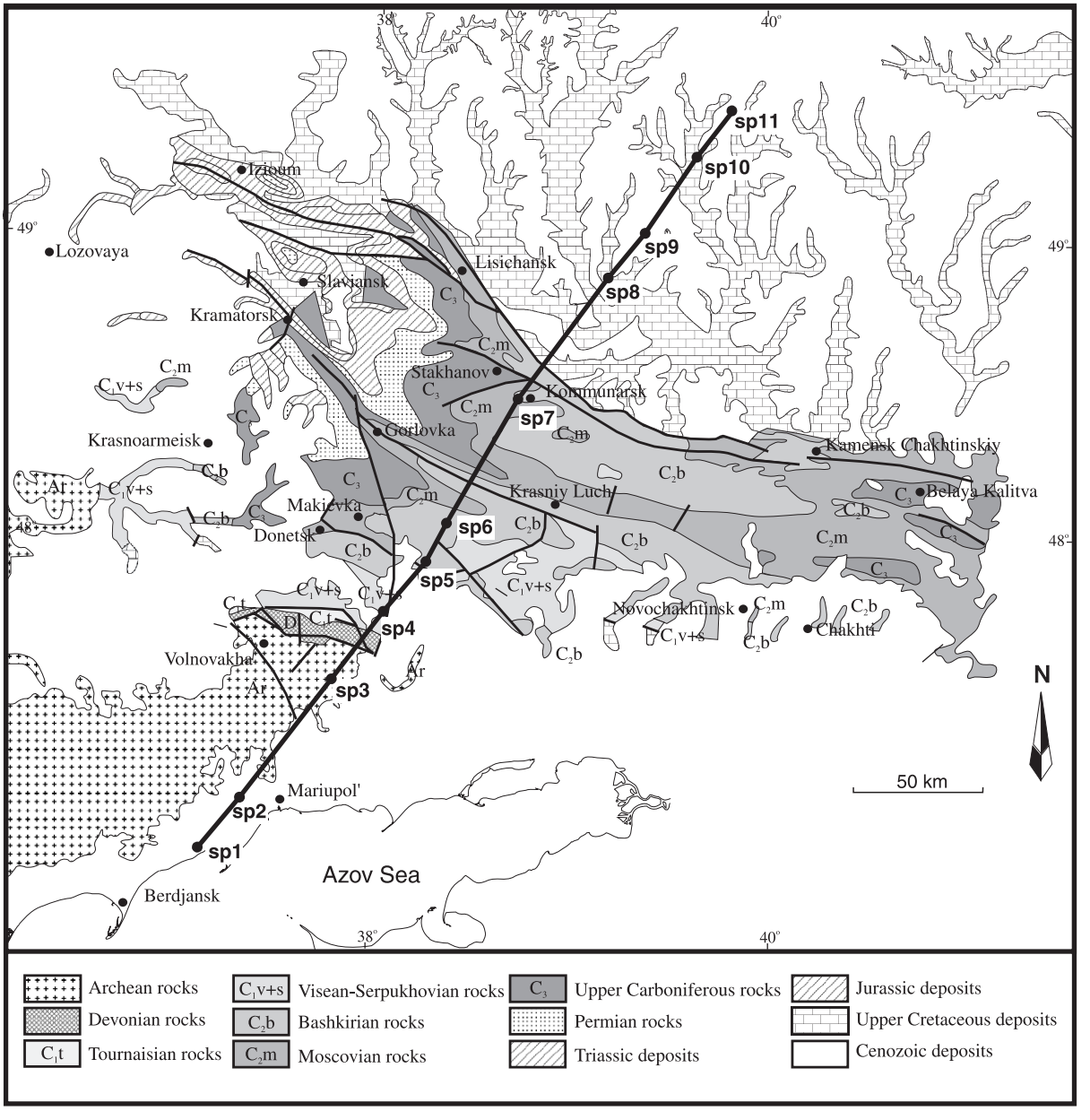

Fig. 2. Geological map (with legend) of the Donbas Foldbelt area with the locations of the DOBREfraction'99 profile and shot points (filled dots with sp1–sp11 labels).

from severe in the DF to practically none in the Dniepr segment. There is a major Permian unconformity, with increasing thicknesses of eroded strata inferred to the southeast, and it had long been regarded that basin "inversion" was related to Permian (Variscan/Uralian) orogenesis on the margins of the EEC. Several kilometres of mainly Carboniferous strata have been eroded in the DF, especially on its southern margin (e.g. Stovba and Stephenson, 1999). This is evident in the geological map included as Fig. 2. What little is known about the subsurface structure of the DF has been based on surface exposure and shallow boreholes, the latter almost exclusively to depths less than 1000 m (Stovba and Stephenson, 1999). This has been augmented by new deep seismic reflection data (cf. DOBREflection-2000 and DOBREfraction'99 Working Groups, 2002; Maystrenko et al., in press). In any case, the Late Palaeozoic and younger sedimentary succession in the DF is more than 20 km thick and most of this is of Carboniferous age.

The driving mechanism of rifting causing the DDB remains a matter of speculation (Stephenson et al., 2001). Voluminous magmatism and some modelling inferences are suggestive of mantle plume influence (e.g. Wilson and Lyashkevich, 1996; Kusznir et al., 1996a,b) but whether an upwelling plume caused the rifting or vice versa is unresolved. An analogy with "back-arc" magmatism within the roughly contemporaneous Variscan geosynclinal system has also been proposed (Nikishin et al., 1996). In this case, DDB rifting is thermomechanically related to convergence on the southern margin of the EEC (leading to accretion of the Scythian "plate"). Alternatively, intracratonic rifting within a larger craton, leading ultimately to continental break-up and development of the present southern margin of the EEC in the Devonian, with the DDB being a failed arm of such a rift system, has also been proposed (Zonenshain et al., 1990).

Similarly, the mechanisms leading to uplift and compressional deformation in the inverted (DF) part of the DDB are also unknown. The geological setting of the DF is complicated by the variable proximity of the basin axis to the inferred southern edge of the EEC and its presumed relationship with contemporaneous basin development on the southern (Scythian) margin of the EEC. Seismic reflection data in the southeastern DDB (Donets segment) reveal that the Late Palaeozoic reactivations (syn-Variscan/Uralian) were mainly (trans)extensional rather than compressional whereas compressional deformation took place at the end of the Triassic and, more intensely, at the end of the Cretaceous (Stovba et al., 1996; Stovba and Stephenson, 1999). Post-rift reactivations increase toward the southeast and it can be surmised that they were even more profound in the DF than in the uninverted part of the DDB. Recent geological mapping and paleostress analysis also suggest that the main compressional tectonic events forming the present structure of the DF took place in the Mesozoic and early Cenozoic (Saintot et al., in press).

A regional refraction/wide-angle seismic survey in the DF was carried out in August–September 1999 (DOBREfraction'99) as an integral part of a multidisciplinary study of the DDB and DF initiated by the European Science Foundation EUROPROBE Programme (cf. Gee and Zeyen, 1996). The survey comprised a main profile of length ~360 km crossing the western DF and a subsidiary, parallel, off-line profile about 100 km to the west in the DF (Fig. 2). The main profile extends to the south across the Azov Massif to the shores of the Azov Sea and to the north onto the Voronezh Massif. Within the general objectives of the EUROPROBE programme aimed at understanding the mechanisms of intraplate tectonics and sedimentary basin dynamics, the immediate goals of DOBREfraction'99 were to map out the fundamental deep structure of the DF relating this to the processes of rift basin formation and eventual inversion.

2. Previous DSS studies of the Donbas Foldbelt

Available data on the crustal structure of the DDB and DF include some 13 Deep Seismic Sounding (DSS) profiles across the rift, spaced at intervals of 50–150 km, one longitudinal profile, and several on the flanks of the rift (Fig. 1). Most of these studies took place in the 1960s and involved high-density (100 m station spacing) recording of seismic arrivals with maximum offsets of 60–160 km and were primarily designed to determine intrabasinal and intracrustal structure. The depth to the base of the crust

was interpreted mainly from secondary (reflected) phases in the offset range 35–40 km and greater (e.g. Borodulin and Khokhlov, 1970a,b). In general, these studies provided a good indication of the disposition of the basement surface (top of the "consolidated crust") and a first-order indication of intrabasinal geometry.

P-wave velocity models along these profiles were constructed during the last three decades using various techniques. No S-wave velocity models exist. Prior to 2000, no crustal scale deep seismic-reflection profiles were recorded across the DDB or DF. Some recently published velocity models can be seen in Pavlenkova (1995), Ilchenko (1996), and Stephenson et al. (2001). These indicate that the Moho is several kilometres shallower beneath the axis than the flanks of the basin in the Dniepr segment of the DDB, but is almost horizontal in the Donets sector. In turn, the thickness of the sub-sedimentary layer crust decreases from 30–35 to 20–25 km, respectively. The Moho was thought to deepen beneath the DF (Chekunov et al., 1992; Stephenson et al., 1993, 2001). Crustal velocities are higher beneath the rift than beneath flanking areas and, in the Donets segment, a crust–mantle transition zone with velocities of about 7.6 km s^{-1} overlies upper mantle (8.0 km s^{-1}). It should be noted, however, as clearly demonstrated by Ilchenko (1996), that velocities beneath the upper crust, including those of the high velocity "crust–mantle" lens, are poorly constrained (being not controlled by refracted seismic phases) in all of the earlier data sets.

DSS profiles of immediate interest to the DF include those that are labelled in Fig. 1: profiles X (Nogaisk-Konstantinovka-Svatove), XI (Novoazovsk-Lugansk-Titovka), XII (Mechebilovo-Artemovsk-Sverdlovsk), and XIII (Guliaipole-Gorlivka). The first of these was observed in 1965 (cf. Garkalenko et al., 1970) and the other by the industrial exploration organisation Dniprogeofizika in the years 1967–1971 (cf. Garkalenko and Borodulin, 1972; Borodulin and Mikhalev, 1973; Borodulin, 1978). In the central part of the DF, where the sedimentary layer is more than 20 km thick, a number of distinct, intrasedimentary seismic horizons was identified (Garkalenko and Borodulin, 1972) but little could be observed of the structure of the underlying crust. The former were correlated with the horizons separating Mesozoic and younger strata (1.8–2.2 km s^{-1}) from the Carboniferous succession (4.0–5.0 km s^{-1}) and with certain horizons within the Carboniferous. Basement velocities were observed in the range 6.3–6.7 km s^{-1}. On the southern flank of the DF a lower crustal layer with an apparent velocity of 6.5–7.0 km s^{-1} was inferred on the basis of both reflected and refracted phases. Reflected phases interpreted to be from the Moho surface as well as from horizons within the upper mantle were recorded at offsets greater than 70–90 km (up to the 160 km maximum). In general, the inferred P_MP phase (Moho reflection) is rather distinct.

These DSS data were used over a number of years to establish a working hypothesis of crustal blocks in the DF area, including determination of

Table 1
DOBREfraction'99 shot points

Shot point	Latitude [°N]	Longitude [°E]	Altitude [m]	Time year:day:hour:minute:second [UTC]	Charge [kg TNT]
SP01	46.9506	37.1794	10	1999:240:20:00:00.000192	800
SP02	47.1240	37.3780	45	1999:240:21:30:00.000190	700
SP03	47.5320	37.8145	90	1999:240:22:00:00.000195	400
SP04	47.7641	38.0638	96	1999:240:21:00:00.000162	400
SP05	47.9346	38.2702	90	1999:240:22:30:00.000224	400
SP06	48.0655	38.3696	135	1999:241:20:30:00.000163	400
SP07	48.4869	38.7185	156	1999:242:21:30:00.000224	400
SP08	48.8988	39.1686	52.5	1999:242:21:00:00.000169	400
SP09	49.0498	39.3552	138	1999:242:20:30:00.000189	600
SP10	49.3069	39.6182	69.5	1999:242:20:00:00.000209	700
SP11	49.4637	39.8030	138	1999:241:23:00:00.000192	1050

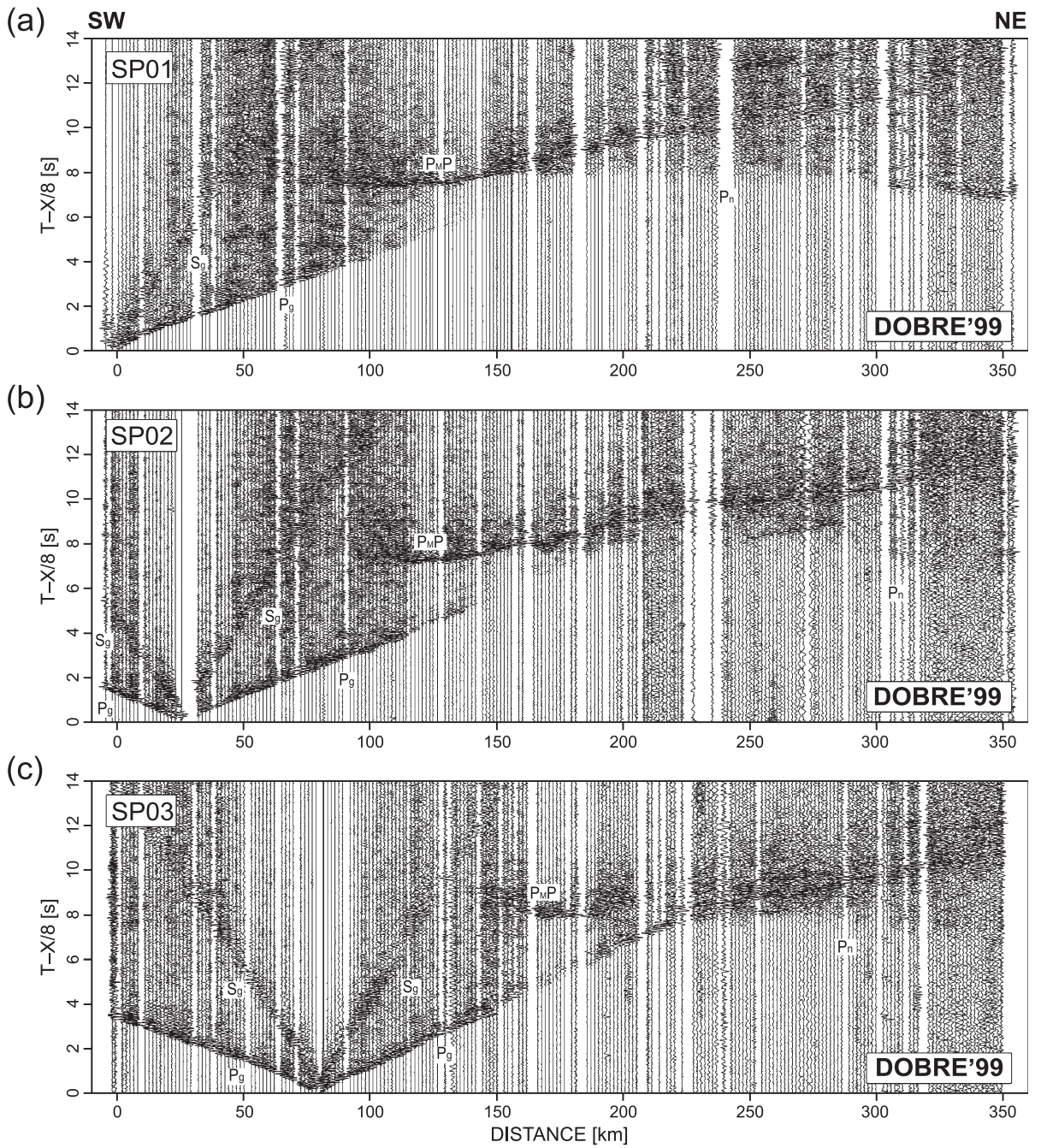

Fig. 3. Amplitude-normalised seismic record sections for (a) SP01, (b) SP02, (c) SP03, (d) SP04, (e) SP05, (f) SP06, (g) SP07, (h) SP08, (i) SP09, (j) SP10, and (k) SP11; reduction velocity 8.0 km s^{-1}. Abbreviations used (see text): Psed and Ssed-P and S refracted arrivals from the supracrustal (sedimentary) layer; Pg and Sg—P and S refracted arrivals from the upper crust; $P_{HVB}P$—reflected arrivals from a lower crustal high velocity body (HVB); Pn—sub-Moho refraction; P_MP and S_MS—P and S reflected arrivals from the Moho discontinuity, P^{II}—reflection from within the upper mantle.

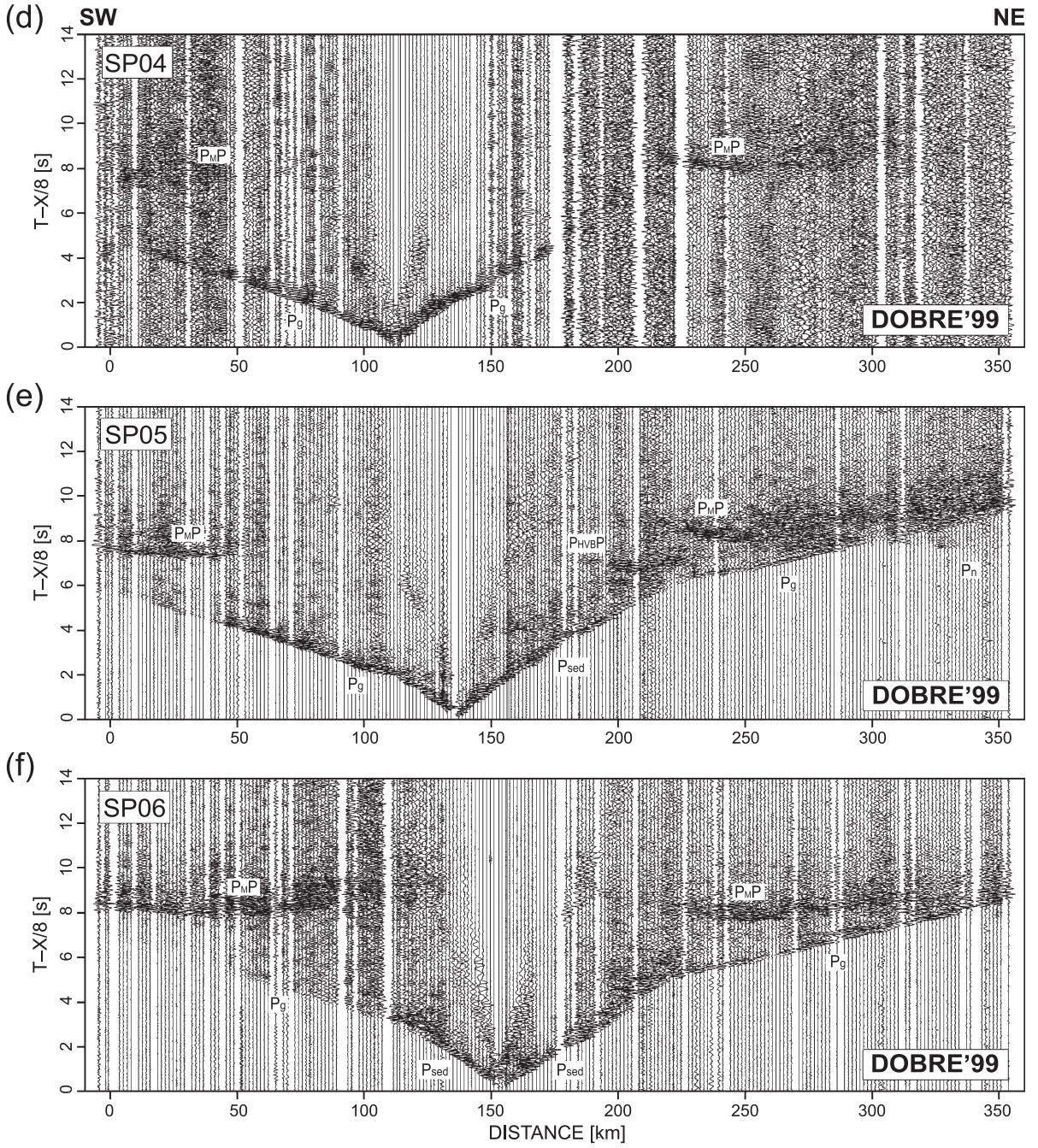

Fig. 3 (*continued*).

the regional geometry of the crystalline basement and Moho surfaces (e.g. Sollogub et al., 1977; Chekunov et al., 1992; Ilchenko, 1992; Ilchenko and Stepanenko, 1998). Integration with other geophysical and geological data allowed various tectonic schemes to be proposed for the DF and its

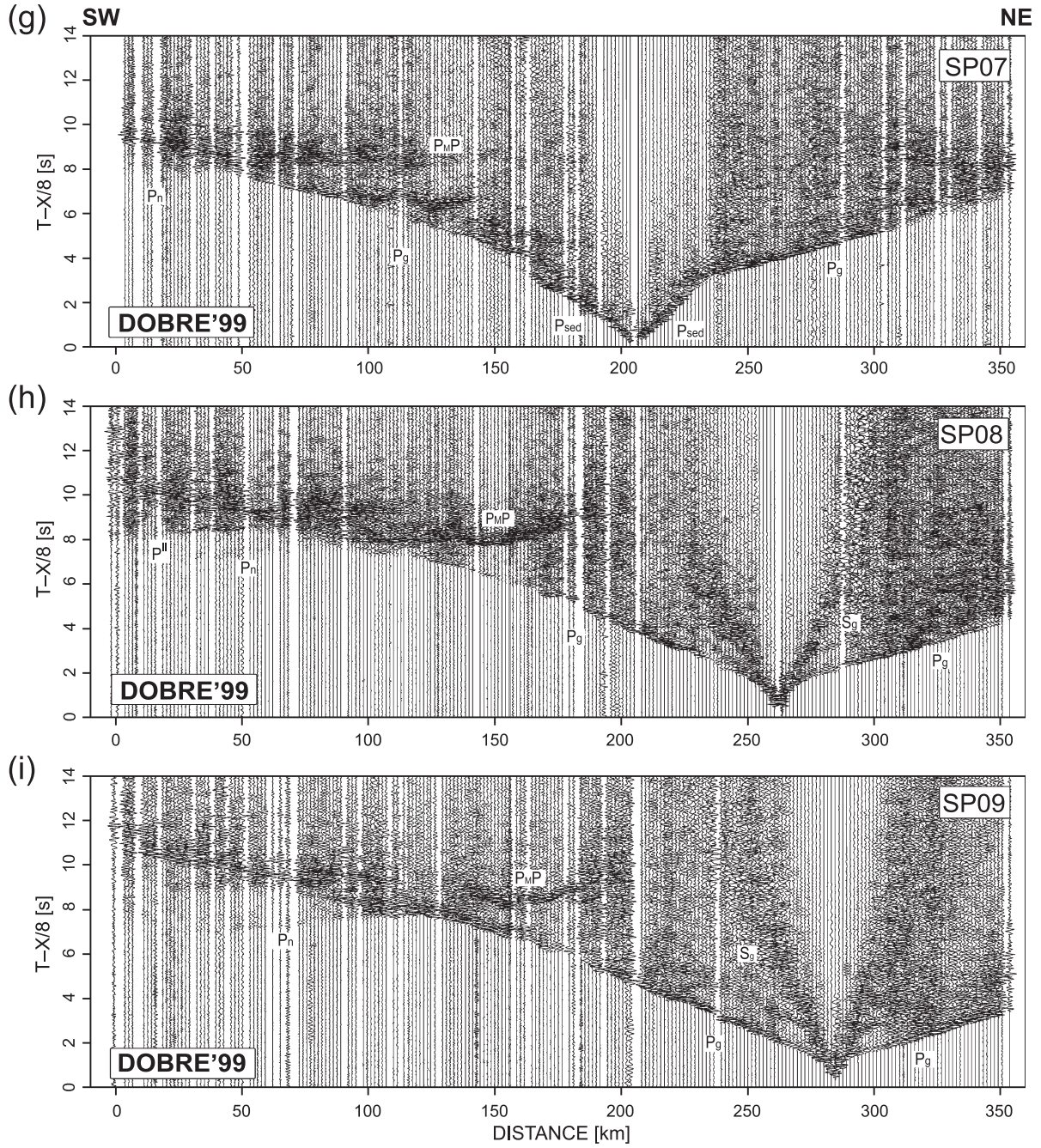

Fig. 3 (*continued*).

main structures and for contiguous structures (e.g. Garkalenko and Borodulin, 1972). Nevertheless, even though the DF is a well-studied, major coal basin, there exists to this day no common view as to its origin, evolution, overall structure at depth and the nature of its along-strike transition to the

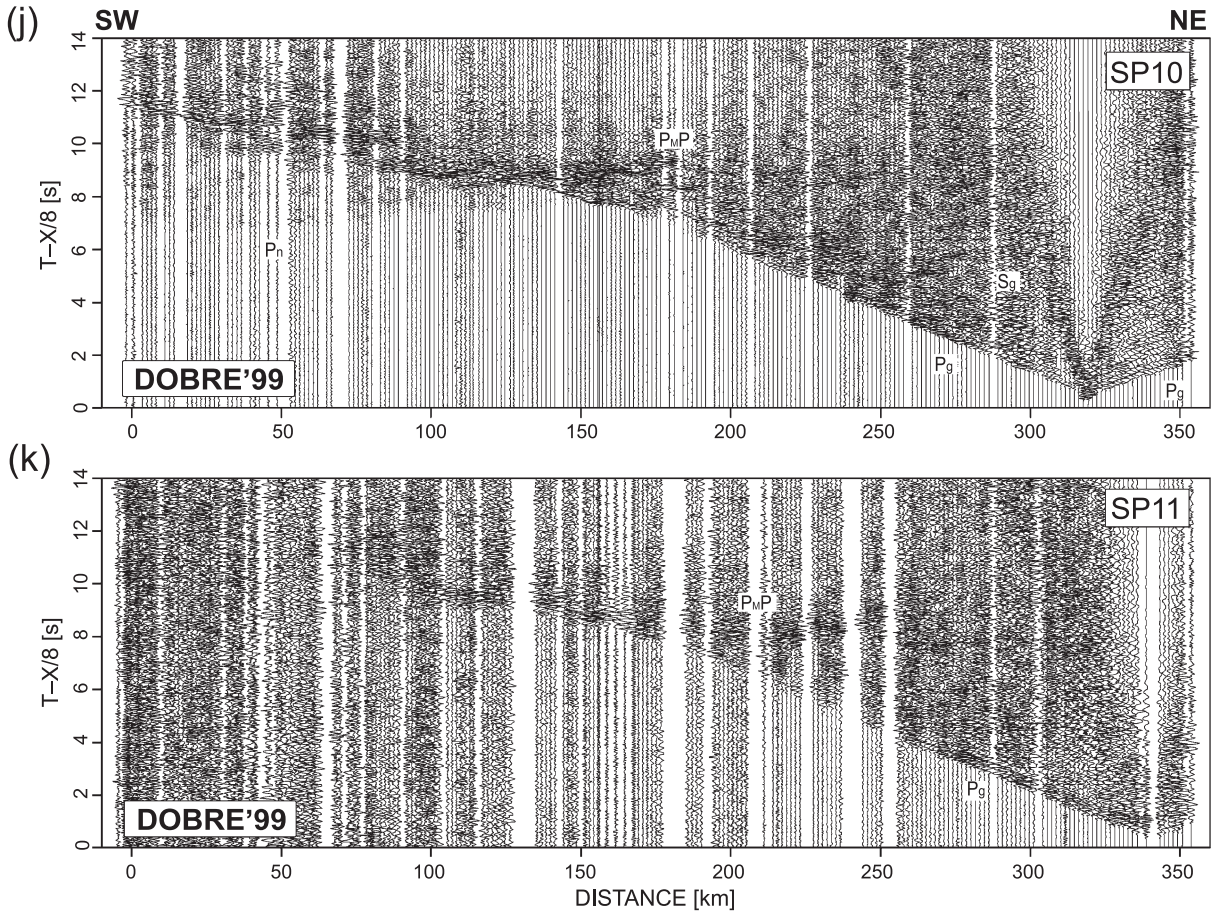

Fig. 3 (*continued*).

uninverted DDB (northwest) and the Karpinsky Swell (southeast).

3. DOBREfraction'99 survey and data

The DOBREfraction'99 refraction/wide-angle data were recorded using autonomous one-component digital seismic stations, mainly REFTEK-125s (''Texans'') from the University of Texas at El Paso and the University of Copenhagen, augmented with 20 digital three-component stations of the Institute of Geophysics of the Polish Academy of Science. There were 245 of these placed along the 359 km long main DOBREfraction'99 profile and 36 stations on a 190 km long subsidiary fan profile, all recording 11 shots placed in-line every 25–30 km along the main profile (Fig. 2). Nominal station spacing was 1.5 and 5 km, respectively. Shot point attributes are summarised in Table 1. Positioning and timing was accomplished using GPS. The fieldwork was carried out in August–September 1999 by the Institute of Geophysics of the National Academy of Sciences of Ukraine and the state Exploration Company ''Ukrgeofisika'', as well as other participating institutions.

The 11 DOBREfraction'99 main profile shot gathers, plotting with reducing velocity of 8.0 km s^{-1} and amplitude-normalised, are displayed, along with identification of the main recorded seismic phases, in Fig. 3a–k. Shot gathers 1 and 3 are replotted in Fig. 4 with a compressed time scale in order to highlight recorded S-wave phases. Refracted P- and S-wave phases from

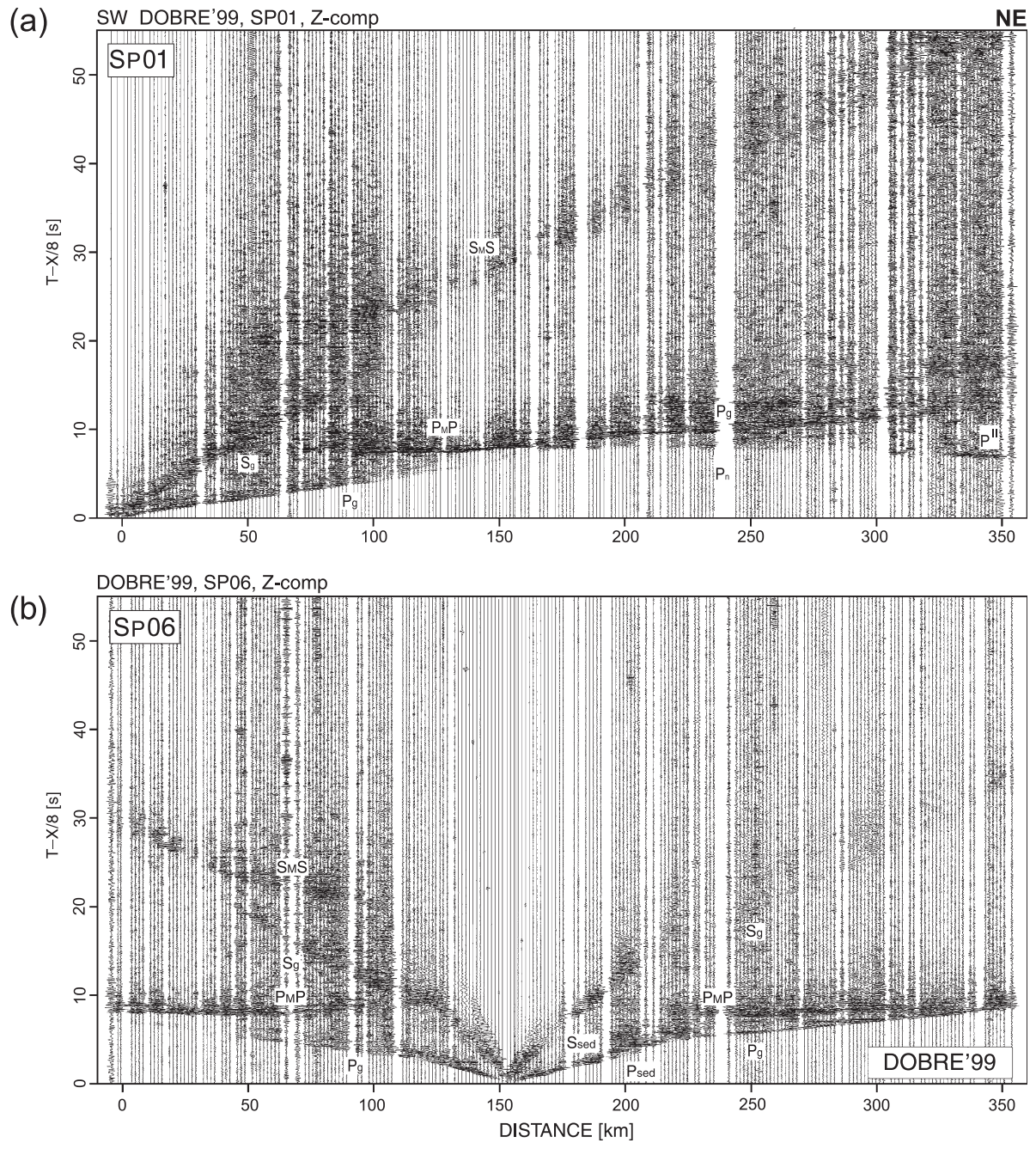

Fig. 4. Amplitude-normalised seismic record sections for (a) SP01 and (b) SP06 (P- and S-waves); reduction velocity 8.0 km s^{-1}; abbreviations as defined in Fig. 3.

horizons within the sedimentary and crustal layers (Psed, Ssed, Pg, Sg) are easily identified, as are reflections (P_MP, from about 70 km offset) and refractions (Pn) from the Moho. Intracrustal ($P_{HVB}P$, Fig. 3e) and intramantle (P^{II}, Fig. 3h) reflected phases are also seen.

The near-offset arrivals display pronounced variation because of the sedimentary graben structure in the central part of the profile. The first arrivals for the most southern and northern shot points are the Pg phase with an apparent velocity of ca. 6.0 km s^{-1}. In contrast, first arrivals (Psed) in the central part of the profile, where it crosses the DF, show smaller velocities, which correspond to the velocities of the supracrustal sedimentary succession. Sedimentary velocities are lowest in the northern part of the basin, where values of around 3.0 km s^{-1} correspond to the expected velocity of the subcropping Cretaceous sedimentary succession. In the main part of the basin, the velocity of the first arrivals are larger, between 4.0 and 5.8 km s^{-1}, which corresponds to sedimentary rocks of the Palaeozoic succession. Secondary phases that may be ascribed to reflectors within the main sedimentary basin structure are observed in several seismic sections (SP05-09; Fig. 3e–i). These phases furnish constraints on the depths to interfaces between sedimentary layers.

The base of the sedimentary basin (top of the crystalline crust) is imaged by reflections on all shot points in the centre of the profile. These reflected phases constrain to a large extent the shape of the basin, although they do not provide total coverage of the basement interface. However, the refracted wave from the upper crystalline crust completes the coverage of the upper crystalline basement, in most parts of the profile with reverse coverage. This phase shows apparent velocities of 6.0–6.3 km s^{-1}, generally highest in the northern part of the profile.

Intracrustal reflections are sparse along the profile. They generally appear as single reflections that may be identified in one or two sections without reverse coverage. These have mainly been modelled (see below) as "floating reflectors", that is, reflectors without any associated velocity contrast within the crust. Such reflectors may image tectonic features or they may be remnants of early lithological contrasts partly destroyed by later metamorphic processes.

The P_MP reflection from the Moho is everywhere a strong, pronounced phase. In many sections it is also embedded in, or marks the onset of, a coda of strong reflectivity that may indicate layering around the base of the crust. The reflectivity from the lower crust and around the Moho is most pronounced for reflection points around the centre of the profile, slightly displaced to the north, and generally absent for reflection points at the ends of the profile. This variation is evident even in single seismic sections (e.g. SP04N and SP09S; Fig. 3d–i). The Pn phase is observed in all seismic sections with an apparent velocity of 8.0 to 8.3 km s^{-1}, highest for arrivals in the northern part of the profile.

A strong secondary arrival is observed in a few seismic sections at offsets larger than 220 km (e.g. SP08S; Fig. 3h). It arrives after the Pn phase, which shows that its origin must be in the upper mantle. It is interpreted as a reflection from the upper mantle.

The S-wave sections (Fig. 4) show clear arrivals that may be group correlated. These sections mainly show the Sg and S_MS phases, whereas intracrustal phases and mantle reflections cannot be identified with certainty. The combination of the Sg and S_MS phases allows variability in crustal Vp/Vs velocity ratio along the profile to be estimated by keeping the first-order interfaces from the P-wave modelling fixed.

4. Velocity models—results

4.1. Tomographic inversion model

As a first step in the interpretation of the DOBREfraction'99 data set, a tomographic procedure (Hole, 1992) was applied to invert the travel times of the seismic first arrivals (a total of 2119 picks were used) in order to determine quickly and "objectively" a smooth 2D velocity–depth model. The results of this procedure are shown in Fig. 5a, along with an indication of the ray coverage controlling the tomographic model (Fig. 5b).

The method iteratively applies perturbations to a user-defined starting velocity–depth model. The resulting model depends to some degree upon the initial model. In the present case, the initial model must have steep velocity gradients in the top 10 km in order to maintain a dense ray coverage there. Thereafter, the inversion proceeds in a stepwise manner according to increasing offsets and correspondingly increased penetration depth of the deepest turning rays. The optimal model determined for a given offset/penetration depth is transferred to the next and step of the iteration series. The offsets, and corresponding smoothing operators, are selected by the user in

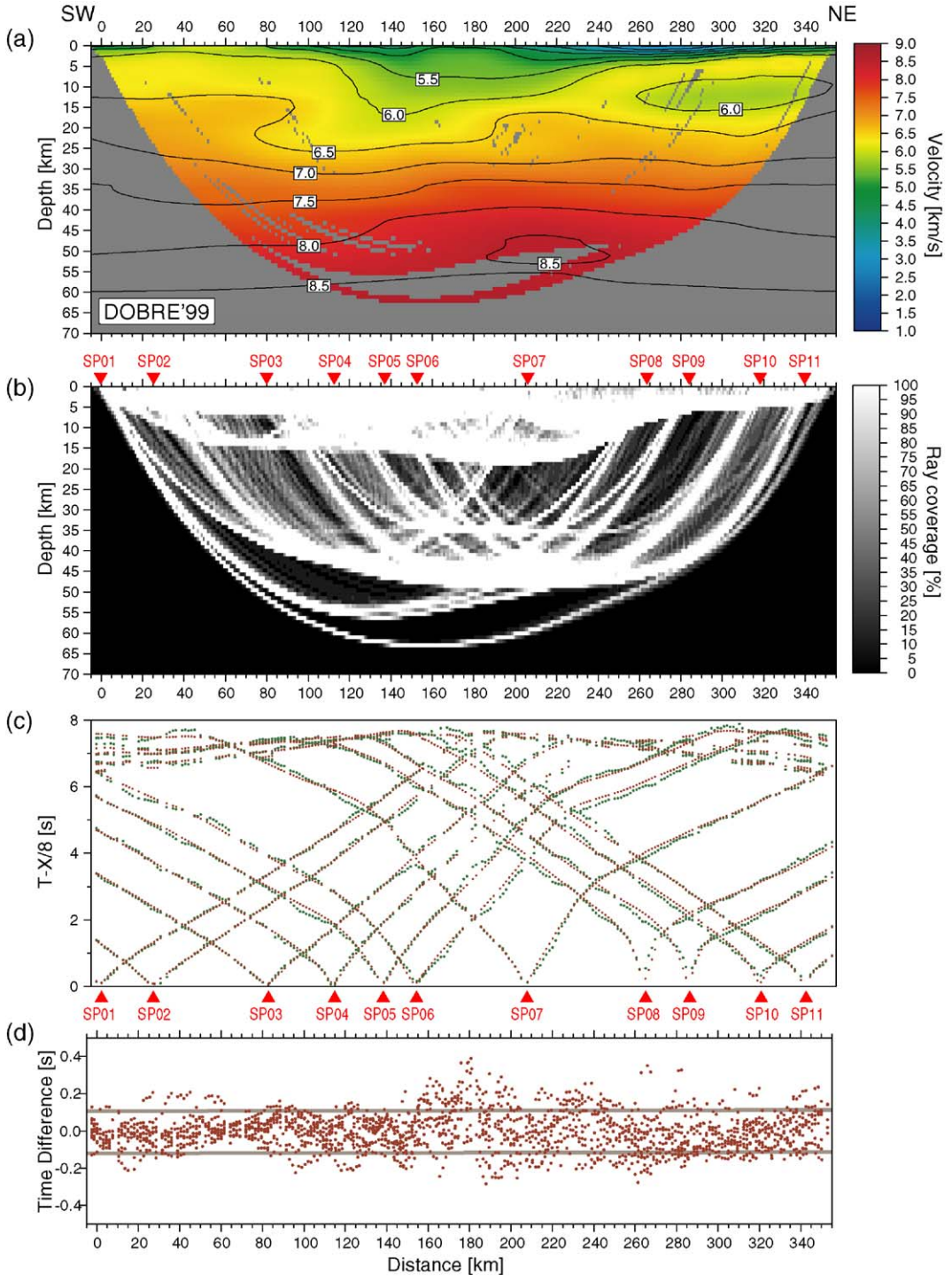
(a)
SW
NE
Depth [km]
DOBRE'99
5.5
6.0
6.5
7.0
7.5
8.0
8.5
Velocity [km/s]
SP01 SP02 SP03 SP04 SP05 SP06 SP07 SP08 SP09 SP10 SP11
(b)
Depth [km]
Ray coverage [%]
(c)
T-X/8 [s]
(d)
Time Difference [s]
Distance [km]

discrete intervals in order to predetermine that rays bottom at significant depths—such as the sediment–crust boundary, the upper, mid- and lower crust as well as the crust–mantle boundary. Travel times of direct, refracted, diffracted or head waves (i.e., first arrivals only) are calculated using a finite difference algorithm based on the eikonal equation (Vidale, 1990). The velocity model is defined on a uniform grid and first arrival travel times, as well as travel time residuals, are computed at all grid points. The number of iterations for the inversion process is determined from the trade-off between the RMS travel time residual and the requirement for a smooth model, as assessed by visual inspection for smoothness versus nonlinearity. The iteration procedure continues until the RMS travel time residual reaches a value equal to, or slightly less than, the picking uncertainty. Further iterations may introduce anomalies produced primarily from the noise inherent in the data.

The picking uncertainty is approximately 50 ms for most of the DOBREfraction Psed and Pg phases and 100 ms for Pn. Calculated reciprocity values suggest an overall uncertainty of 100 ms for the DOBRE data. Maximum offset values were set to 80, 150, 200, 250, 300, 350 and 400 km and for each maximum offset, smoothing operators were selected in four steps as: 120 by 30 km, 60 by 20 km, 30 by 10 km and 20 by 8 km. By using the smoothing operators, some of the nonlinear effects, inherent in any wave propagation problem, are suppressed in the inverse problem. The smoothing filters are applied to derivatives and perturbations but never to the model itself. On average, 6 iterations per offset and smoothing filter were applied, and the average RMS travel time residual for the final model is 99 ms after a total of 143 iterations (Table 2; Fig. 5c,d).

The 11 shots defining the DOBRE profile provide good ray coverage (Fig. 5b) of the main sedimentary basin and the sedimentary succession to the north and south of the basin margins (defined as the area with velocity less than 6 km s^{-1}). The top of the upper crystalline crust and the lowest crystalline crust is also well covered by crossing rays, whereas the middle crust has less dense ray coverage. The presence of low seismic velocities in the thick sedimentary succession underlying the DF is clearly indicated in the resulting tomographic velocity model. There is also a suggestion of Moho shallowing below the sedimentary basin. A low velocity zone (LVZ) is present in the northern part of the calculated model and a high velocity zone (HVZ) is present in the upper mantle at distances in the range 180–250 km. Further testing indicated that a combination of basin geometry and the effect of the large smoothing filters might possibly cause the inferred upper crustal LVZ. The sparse ray coverage of the area yields poor constraints on the velocities in the entire upper crystalline crust north of the sedimentary basin and the lack of crossing rays prevents higher velocities to be inferred by the inversion process during later iterations. The LVZ can be regarded as an end-member solution, which exists in the infinite inverse modelling solution space, but which is not evident in the travel time data.

Table 2
Statistics for modelled and observed first arrivals

Shot	Picks	Modelled picks	Rms residual (ms)	Modelled picks with rms>100 ms
1	179	167	65	24
2	163	153	81	30
3	180	170	75	29
4	145	136	99	33
5	232	222	102	76
6	205	195	126	89
7	225	213	95	57
8	217	207	109	63
9	213	202	109	61
10	218	208	117	75
11	142	131	148	49
Total	2119	2004		#586
Average rms residual			99	

4.2. Ray-trace velocity models

The DOBREfraction data were modelled using ray-tracing techniques by three different groups in-

Fig. 5. (a) Model of seismic compressional velocity, resulting from the 2D tomographic inversion. (b) Ray coverage for the tomographic model. (c) Travel times for observed (green dots) and calculated (red dots) first arrivals for the tomographic inversion model. (d) Misfit between observed and calculated travel times. Less than 30% have an RMS travel time residual larger than 100 ms (shown by the two horizontal lines); average RMS travel time residual is 99 ms. Red triangles indicate the locations of shot points.

volved in the acquisition programme—University of Copenhagen, the Institute of Geophysics of the Polish Academy of Sciences, and the Institute of Geophysics of the National Academy of Sciences of Ukraine. Although a common set of phase identifications and correlations was employed for all three models, the use of different model parameterisations, as well as qualitative (subjective) aspects of the modelling process, were expected to lead to a robust identification of key model characteristics.

The travel times of refracted and reflected P-waves determined by the correlation process provided the basis for the determination of velocity distributions and depths of the seismic boundaries in the crust and uppermost mantle. Sedimentary thicknesses and velocity distribution in the model were initially generalised from borehole information (1–2 km) and earlier high-resolution reflection and refraction seismic surveys that imaged to a depth of ~ 5 km and constrain thin Cainozoic–Mesozoic and uppermost Carboniferous sequences. Based on this information, a preliminary model of the shallow structure was constructed that was only slightly adjusted during the subsequent modelling procedure.

Velocity models were developed using a quasi-inversion approach RayInvr (Zelt and Smith, 1992) as well as two purely forward modelling approaches SEIS83 and Ray84PC, both based on the algorithm of Červený and Pšencík (1983). Fig. 6 displays the three preferred P-wave velocity models based on the different modelling approaches and it is readily seen that similarities among the models are far more prevalent than differences, the latter occurring at a "second-order" level rather than in basic features. In the following sections, the velocity models shown in Fig. 6 are documented and compared to the observed data, in turn, after which the common features of the velocity models will be described and interpreted.

4.2.1. RayInvr model

The 2D model of the seismic P-wave velocity structure of the DF shown in Fig. 6a was constructed by the University of Copenhagen group using the ray tracing and inversion algorithm of Zelt and Smith (1992), which is based on travel times for both refracted and reflected arrivals. The velocity model is defined in terms of layers that are separated by first order discontinuities at user-specified depths. Velocities are defined at the top and bottom of each layer at selected distances along the profile. Velocities between the specified points are interpolated linearly within each layer. Velocity and depth values can be adjusted manually (forward modelling) or by damped least squares inversion.

Preliminary results of the tomographic inversion of the first break travel times formed the background for the crustal and upper mantle velocities. The model was modified in a three step "layer stripping" procedure for each layer, from the surface layer and successively to deeper levels down to the upper mantle. First, manual adjustment and addition of parameters was made (velocities and depths to boundaries). This included identification of the travel time picks that corresponded to the current layer and determination of a sufficient number of model parameters for later inversion. Second, a reasonable fit between observed and modelled travel times was obtained by making adjustments to parameters followed by application of the inversion algorithm to find the optimal damped least squares solution. During the inversion all relevant velocity and depth values for the layer under consideration were allowed to vary. A priori uncertainties of 0.5–1.0 km and 0.15 km s^{-1} were chosen for depth values and velocities, respectively. By adding strong constraints on the inverse solution, an attempt was made to minimise the difference between the final model and the initial model while improving the least squares fit to the data. Third, the inverse solution was evaluated. If the solution failed to produce rays to the underlying layer due to geometrical "corners", or if negative vertical or strong lateral velocity oscillations appeared, the model was manually modified. Such irregularities were mainly found in the shallow layers where few travel times constrained the model or where contradictions in the reciprocity travel times did not permit a geologically reasonable model. The manual modifications led to lateral homogeneity, without increasing the misfit significantly. In a final modelling step, "floating" reflectors (i.e., reflecting boundaries without model velocity changes) were added to explain reflections where first order velocity discontinuities could not be constrained by the data.

The final RayInvr model (Fig. 6a) has 11 layers defined at 170 different spatial positions and eight "floating reflectors". The number of velocity param-

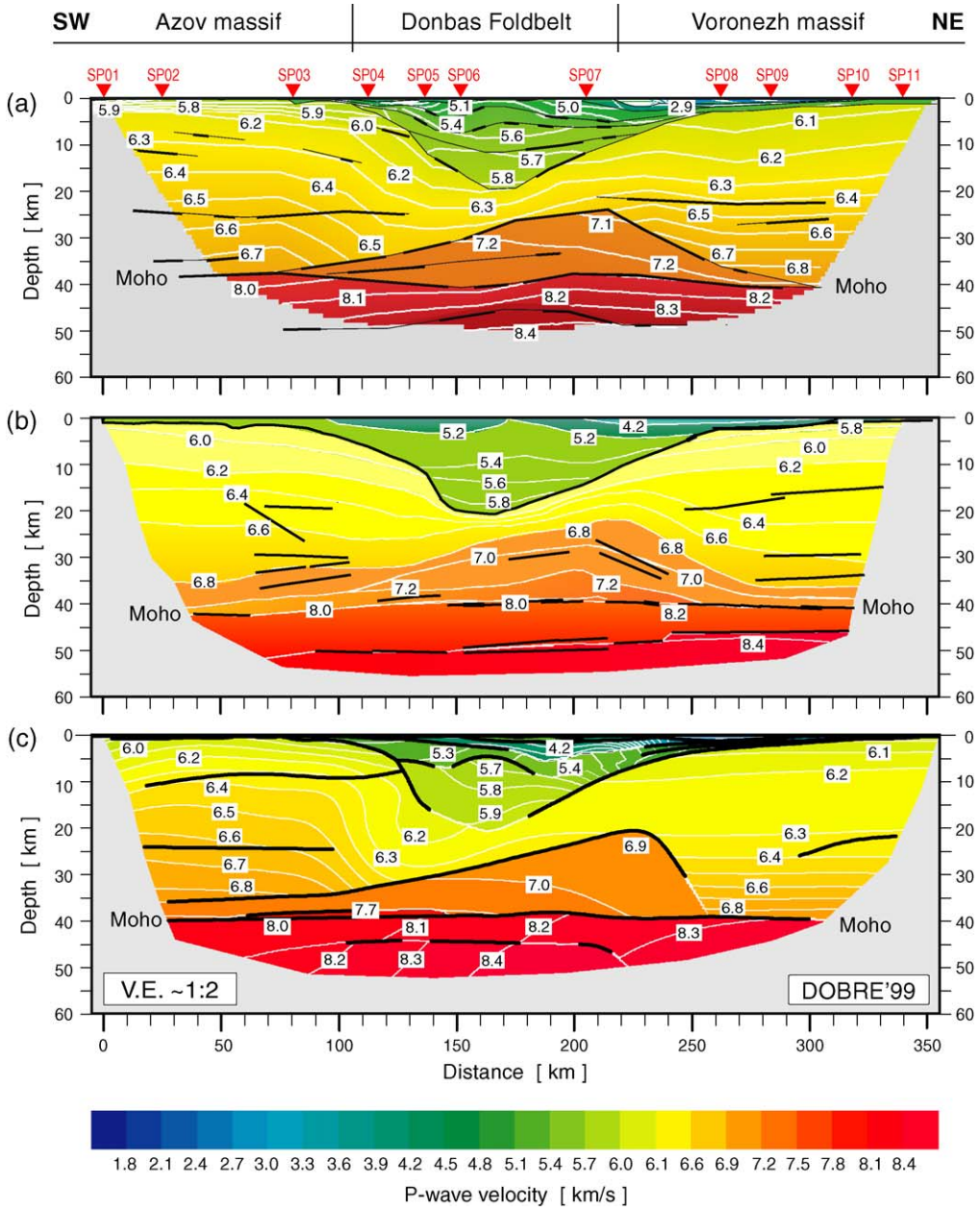

Fig. 6. Colour compilation/comparison of three 2D ray-tracing models. Horizontal axis shows model position; vertical scale is depth below the surface. The velocity field is contoured with a contour interval of 0.1 km s^{-1}. The coloured area is the area traversed by refracted rays, accordingly, the area where velocities are constrained. Layer boundaries and "floating" boundaries are indicated by lines. Thick lines mark positions where rays are reflected, indicating well-constrained boundary positions. (a) RayInvr model; (b) Ray84PC model; (c) SEIS83 model.

eters is 160. Two of the floating reflections, given their depths at 22 to 26 km, indicate a possible separation of the crust into an upper and a lower crust. However, this separation is not supported by a significant change in velocity of the crust. This model reproduced a total of 3190 of the 3600 observed travel times. Geometrical shadow zones in the model cause the relatively low number of travel time hits. The RMS misfit between modelled and observed travel times is 73 ms (between 82 ms for shot 6 and 56 ms for shot 2; cf. Table 3). In general, the misfit is largest for the shots with large differences in reciprocity travel times to other shots (shots 6, 7, and 8). The estimated picking uncertainty is between 50 ms for first arrivals close to the shot, and 100 ms for secondary arrivals and for receivers at large offset where the signal to noise ratio is low.

The reliability of the final model was examined by considering the uncertainty and spatial resolution of representative model parameters such as upper and lower crustal velocity, thickness of the main sedimentary basin, depth to Moho, and depth to the top of the lower crustal body. These can be tested using techniques described by Zelt (1999) both for well constrained parameters covered by reflections and refractions of several shots as well as for poorly constrained parameters. The absolute uncertainty is the variation that is permitted for a parameter from its value in the final model without loosing ray coverage, i.e., loosing rays to stations where travel times have been observed, and without increasing the misfit of travel times significantly. The uncertainty of layer boundary positions varies between 1.5 km at the top of the lower crustal body, where the depth is constrained by reflected and refracted rays from several shots, and 2.5 km at the southern slope of the lower crustal body where the depth is poorly constrained (Fig. 7). The velocity uncertainty varies between 0.1 km s^{-1} in the shallow crust and 0.25 km s^{-1} above the Moho discontinuity. Lateral resolution (i.e., the length scale over which lateral variations are averaged by the data) varies between 40 km in the upper crust and 60 km at the base of the lower crustal body. The lateral resolution at the depth of the Moho is 50 km.

The major features of the model are documented by calculated travel time curves superimposed on the seismic sections and plots of the corresponding ray paths (Figs. 8 and 9). Refracted Psed phases from the

Table 3
Misfit between modelled and observed travel times of the DOBRE profile

Phases	Shot 1		Shot 2		Shot 3		Shot 4		Shot 5		Shot 6		Shot 7		Shot 8		Shot 9		Shot 10		Shot 11		All shots	
	np	RMS	np	RMS	np	RMS	np	RMS	np	RMS	np	RMS	np	RMS	np	RMS	np	RMS	np	RMS	np	RMS	np	RMS
Sediments																								
Refractions, Ps	0	–	0	–	0	–	11	56	58	88	56	84	52	71	24	118	9	105	3	126	0	–	213	87
Reflections, PsP	0	–	0	–	0	–	0	–	28	69	63	68	55	81	0	–	0	–	0	–	0	–	146	73
Total	0	–	0	–	0	–	11	56	86	82	119	76	107	76	24	118	9	105	3	126	0	–	359	82
Pg	120	56	123	51	152	61	70	62	89	80	88	113	84	66	136	84	120	69	98	77	92	62	1172	72
Lower crustal body																								
Refractions, Pi	13	50	12	83	27	50	0	–	20	45	0	–	0	–	38	56	38	89	24	81	0	–	172	69
Reflections, PiP	25	66	11	87	43	36	7	46	40	73	29	28	76	94	59	61	33	86	24	71	20	51	367	70
Total	38	61	23	85	70	42	7	46	60	65	29	28	76	94	97	60	71	88	48	76	20	51	539	70
PmP	70	90	84	52	64	89	38	62	80	78	106	68	48	89	79	68	48	82	48	82	42	68	707	75
Pn	58	96	34	67	24	41	13	41	29	54	20	59	13	64	37	57	37	45	72	70	2	71	339	67
All phases	255	68	264	56	309	68	135	68	343	77	384	82	345	78	411	74	304	73	284	72	156	64	3190	73

np, number of picks; RMS, root mean square travel time residuals (ms); Pg, refracted arrival from upper crust; PmP, reflection from the Moho; Pn, sub-Moho refractions.

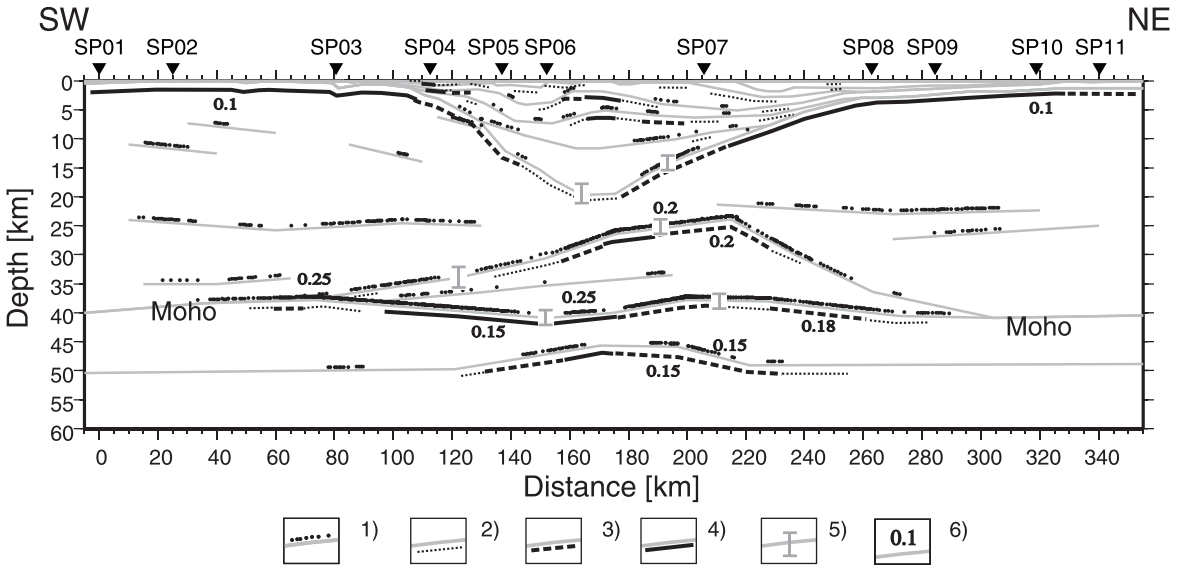

Fig. 7. Illustration of the resolution of the RayInvr model, based on the ray coverage for refracted and reflected phases. (1) Ray reflection point; (2) single shot coverage of refracted rays; (3) one-way coverage by refracted rays from multiple shots; (4) reverse coverage of refracted rays; (5) absolute uncertainty of single parameter depth definition; and (6) absolute uncertainty of a single velocity definition (km s^{-1}).

sediments in the main basin with relatively low apparent velocity and early PsedP reflections (Fig. 8a,b) have been used for subdividing the basin fill into six layers. Velocities range from 2.2 km s^{-1} at the surface in the northeastern part and increase stepwise to 5.8 km s^{-1} in the deepest part of the basin. Large scale apparent folding of these sedimentary layers is observed in the upper part of the basin, resulting in a complex pattern of dipping reflections and variations in the apparent velocities of the refractions. The overall shape of the basin has been modelled on the basis of a strong PsedP reflection observed in shots 5 and 7 (Fig. 8) as well as refractions entering the basin from the northeast and southwest. The dip of the southwestern slope of the basin is 17° on average and has mainly been determined by Pg refractions, since no reflections are observed from the lower part of the basin. The general dip of the northeastern slope is 12°, which is well constrained by PsedP reflections as well as by the Pg phase arriving into the basin from the north. The depth of the basin is almost 20 km. There are no observed reflections from the deepest part, resulting in a high absolute uncertainty on the order of 2 km.

The velocity of the upper crust has been determined primarily from travel times of Pg arrivals for shots located towards the ends of the profile. Dense ray coverage has offered good constraints. Pg travel time curves south of the sedimentary basin display some concavity (Fig. 9a–c), indicating a relatively steep vertical gradient of upper crustal velocities in the southwestern part of the profile, with average velocities of 5.8 km s^{-1} at the surface and 6.2 km s^{-1} at a depth of 4 km. In the northern part of the profile, the uppermost crustal velocities are generally higher, 6 km s^{-1} on average. Mid-crustal velocities of 6.2–6.4 km s^{-1} beneath the basin are constrained by the slope of supercritical crustal $P_{HVB}P$ reflections as well as secondary Pg phase arrivals (Fig. 9b,c). The P-wave velocities of 6.8–6.9 km s^{-1} in the lower crust at both ends of the profile are mainly constrained by the slope of strong supercritical P_MP reflections. A high velocity body is present in the crust beneath the basin, at a minimum depth of 23.5 km. Its shape is defined by relative weak $P_{HVB}P$ reflections (Fig. 9b,c). Velocities from the upper part of the body are 7.1 km s^{-1}, and have been modelled from the Pi refracted arrival. The velocity is well constrained by shots from northeast and southwest, providing good reverse coverage (Fig. 9b,c). The velocity in the lower part of the high velocity body is 7.3 km s^{-1}; it is constrained by wide-angle P_MP reflections. The depth to the Moho is

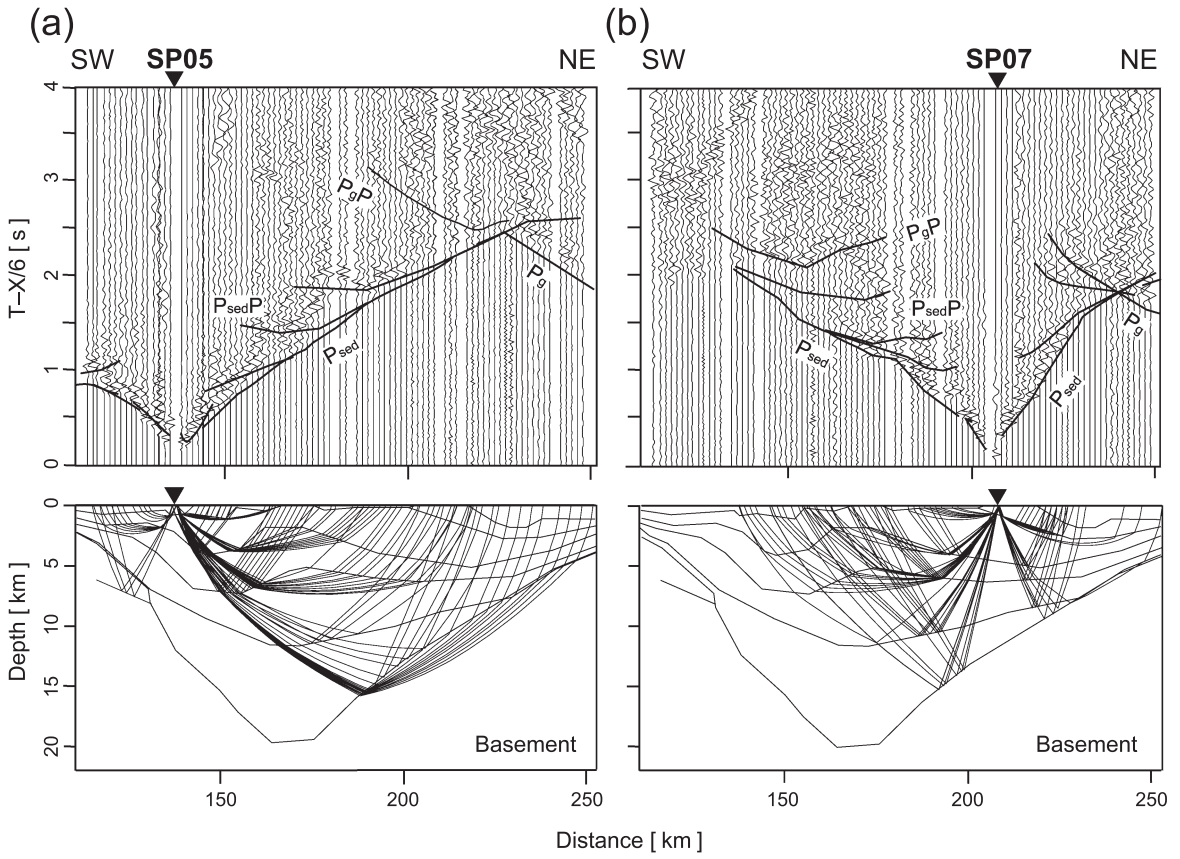

Fig. 8. Ray paths (source to observation point) and calculated travel time curves superimposed on the observed seismic sections for the shallow, sedimentary basin, part of the RayInvr model for shots (a) SP05 and (b) SP07. Horizontal axis shows model position; vertical axis is time with reducing velocity 6 km s^{-1} (upper panel) and depth below the surface (lower panel). Layer boundaries and floating reflections are indicated by lines. For improved clarity, only every third ray is shown reasons. No band-pass filtering has been applied to the seismic traces, but some are left out. Abbreviations used (see text): Psed and Pg—P refracted arrivals from the supracrustal (sedimentary) layers and from rays turning in the upper crust; PsedP and PgP—reflected arrivals from intrasedimentary and basement horizons.

constrained by sub-critical and critical P_MP reflections from all shots (Fig. 9b,c). The average depth is 38 km, but the interface is undulating between 37 and 41 km depth below the lower crustal body. The Pn refractions from the uppermost mantle are generally weak, and display a wide range of apparent velocities from 8.0 to 8.5 km s^{-1} (Fig. 9b,c), indicating structural inhomogeneity. The velocity of the uppermost mantle increases from 8 km s^{-1} in the southwest to 8.2 km s^{-1} in the northeast. The upper mantle is divided into two layers by a first order discontinuity. This separation is based on late P^IP reflections observed on

Fig. 9. Ray paths (source to observation point; lower panel), calculated travel time curves superimposed on the observed seismic sections (centre panel), and synthetic seismic section (upper panel) for shots (a) SP01 for the SEIS83 model, (b) SP03 and (c) SP08 for the RayInvr model and (d) SP09 for the SEIS83 model (Figs. 6a,c). Horizontal axis shows model position; vertical axis is time with reducing velocity 8 km s^{-1} (upper and centre panels) and depth below the surface (lower panel). Layer boundaries and floating reflections are indicated by lines. For improved clarity, only every third ray is shown reasons. Band-pass filtering (2–15 Hz) has been applied in (a) and (d) but no filtering has been applied to the seismic traces in (b) and (c), although some traces are left out. Abbreviations used (see text): Pg—refracted arrivals from the upper crust; PgP—reflected arrivals from the basement; PfP—reflected arrivals from "floating" boundaries within the crust; P_{HVB}—refracted arrivals from the high velocity lower crustal body (HVB); $P_{7.75}$—refracted arrivals from bottom of the HVB, with velocity ~ 7.75 km s^{-1}; Pn—sub-Moho refraction; P_MP—reflection from Moho discontinuity; P^IP and P^{II}—reflections from the mantle.

several shots (Fig. 9b,c) and a change in the apparent velocity of the Pn phase. The velocity below this discontinuity is estimated to be 8.4 km s^{-1}, although the difference in the velocities across the discontinuity is less than the absolute uncertainty of the velocity parameters of the upper mantle.

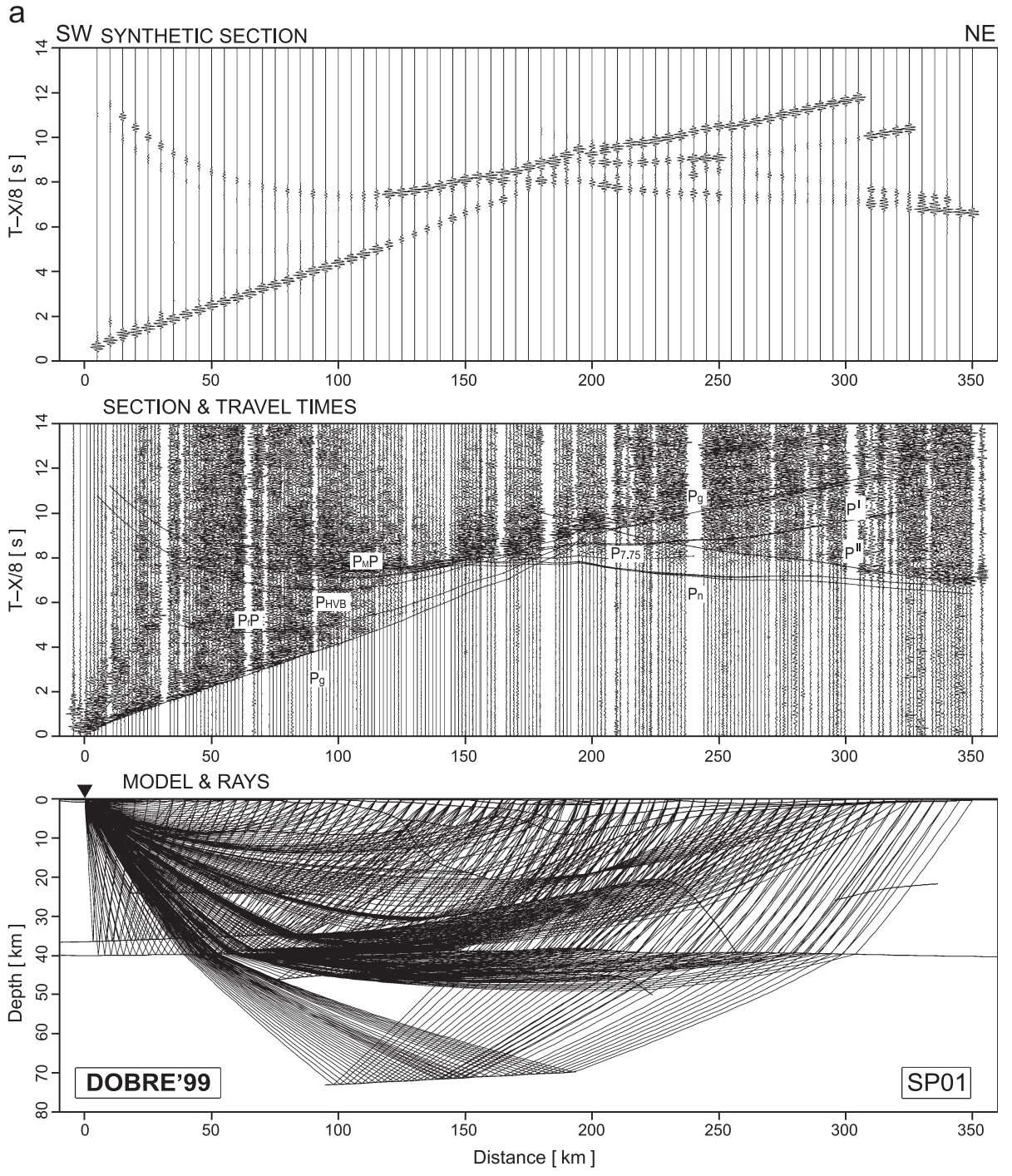

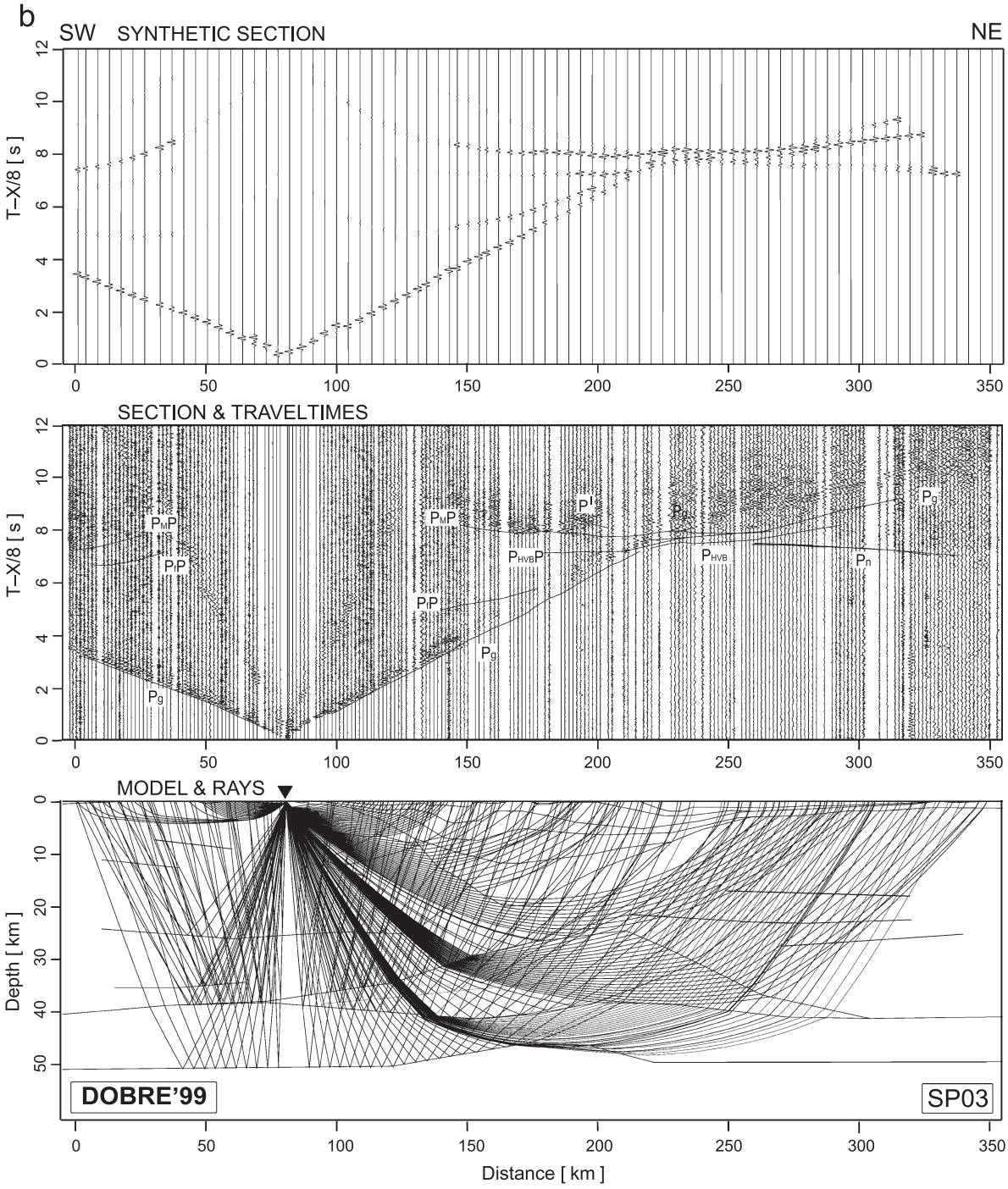

Fig. 9 (*continued*).

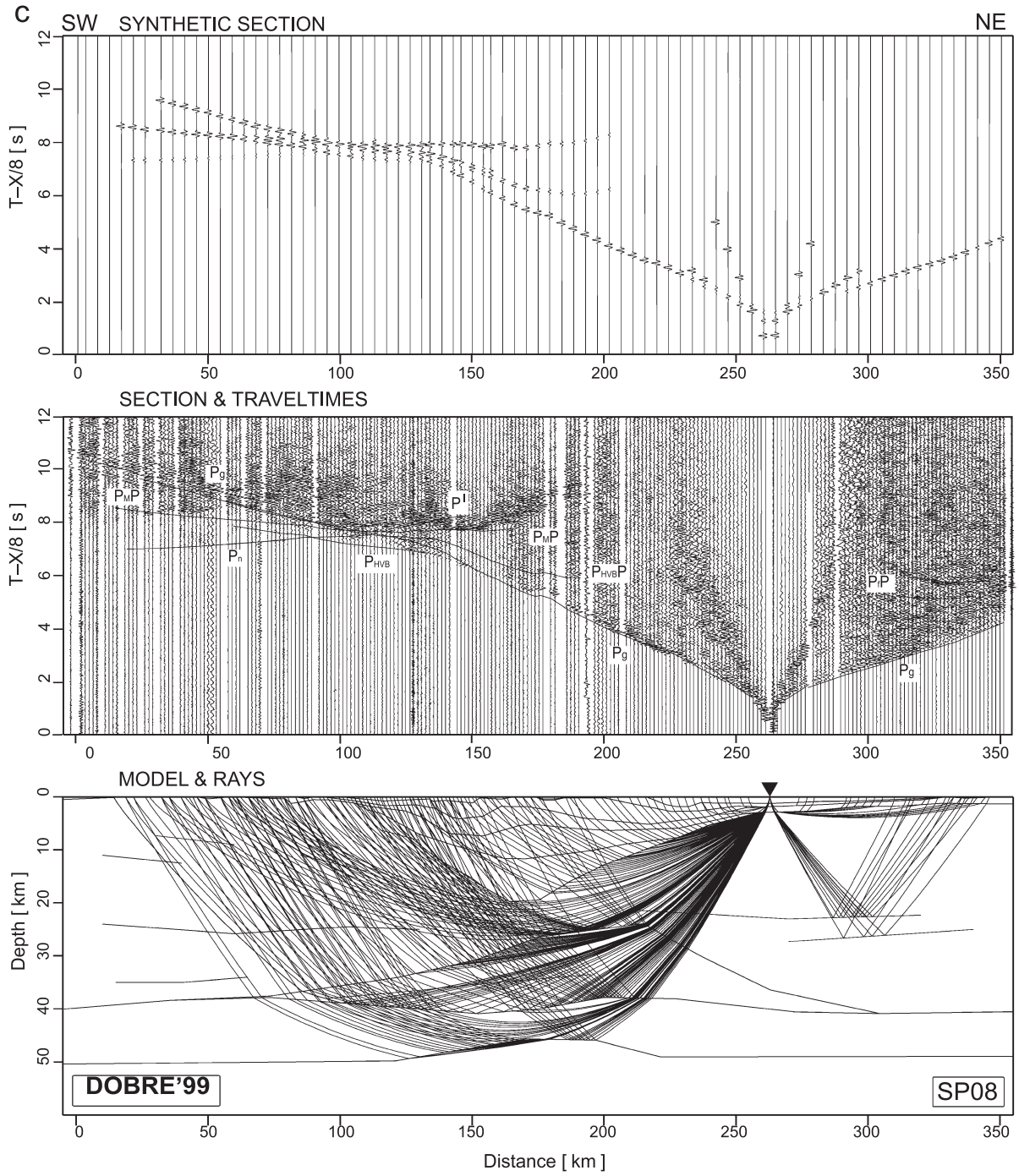

Fig. 9 (*continued*).

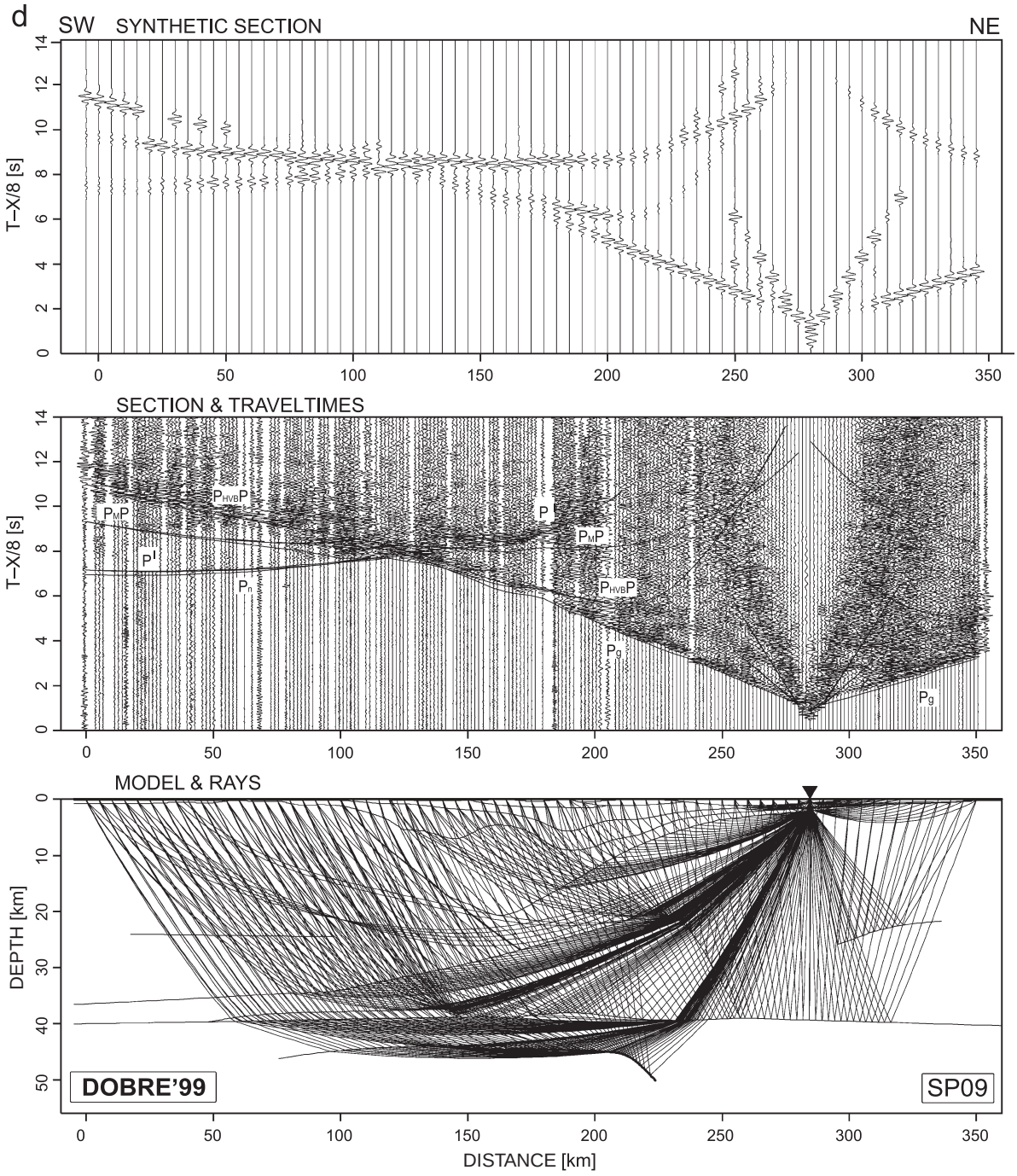

Fig. 9 (*continued*).

4.2.2. Forward ray-tracing models

The forward model using Ray84PC (Thybo and Luetgert, 1990) is shown in Fig. 6b (Institute of Geophysics, Kyiv). It was derived from travel times of direct waves in the sedimentary cover, reflected waves from two discontinuities within the sedimenta-

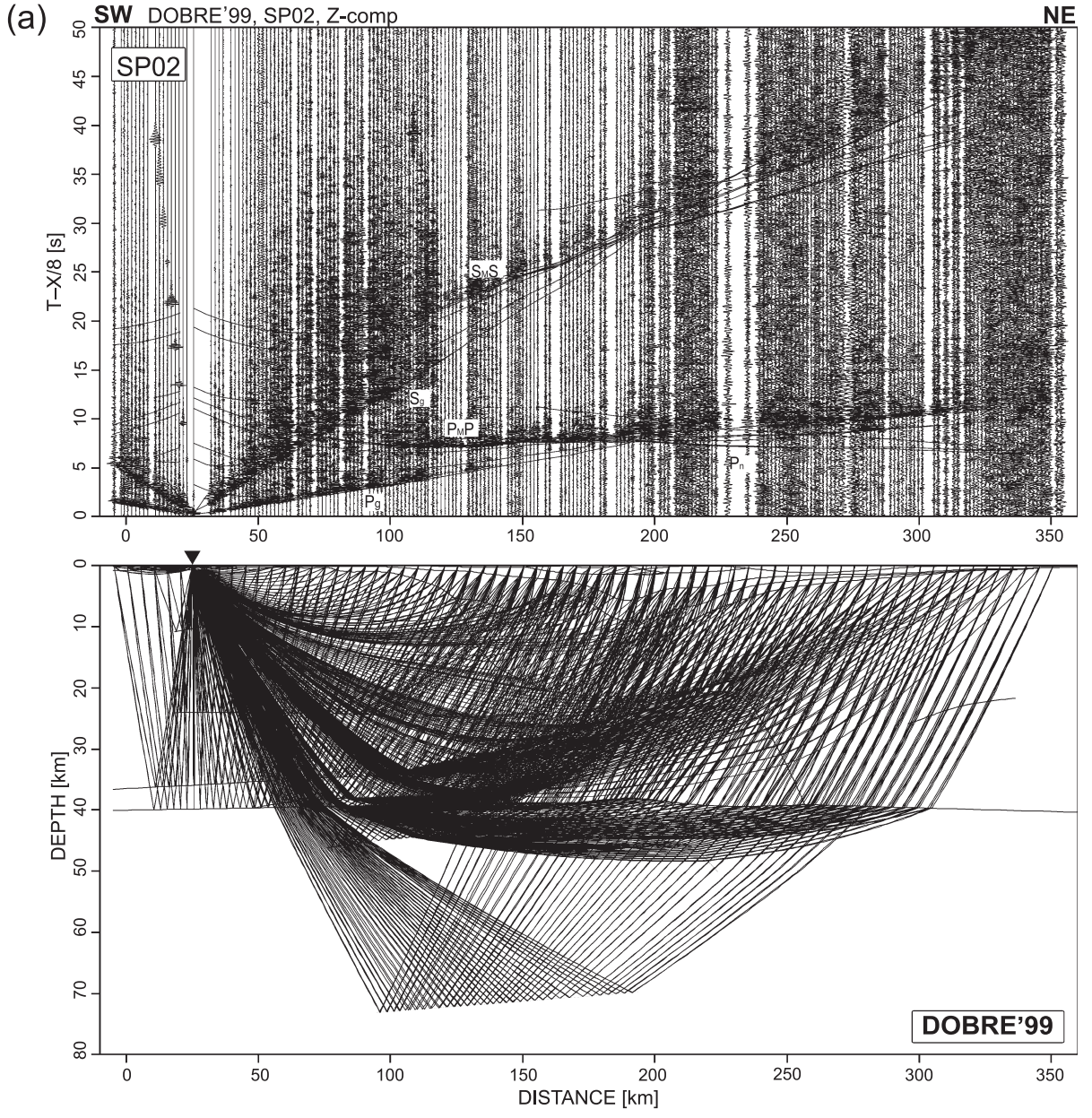

Fig. 10. Ray paths (source to observation point; lower panel) and amplitude-normalised seismic record sections and theoretical travel times of P- and S-waves (upper panel) for the SEIS83 crustal model for shots (a) SP02 and (b) SP10. Abbreviations: Pg and Sg—P and S refracted arrivals from the upper crust, Pn—sub-Moho refraction, P_MP and S_MS—P and S reflections from Moho discontinuity, P^{II}—reflection from mantle.

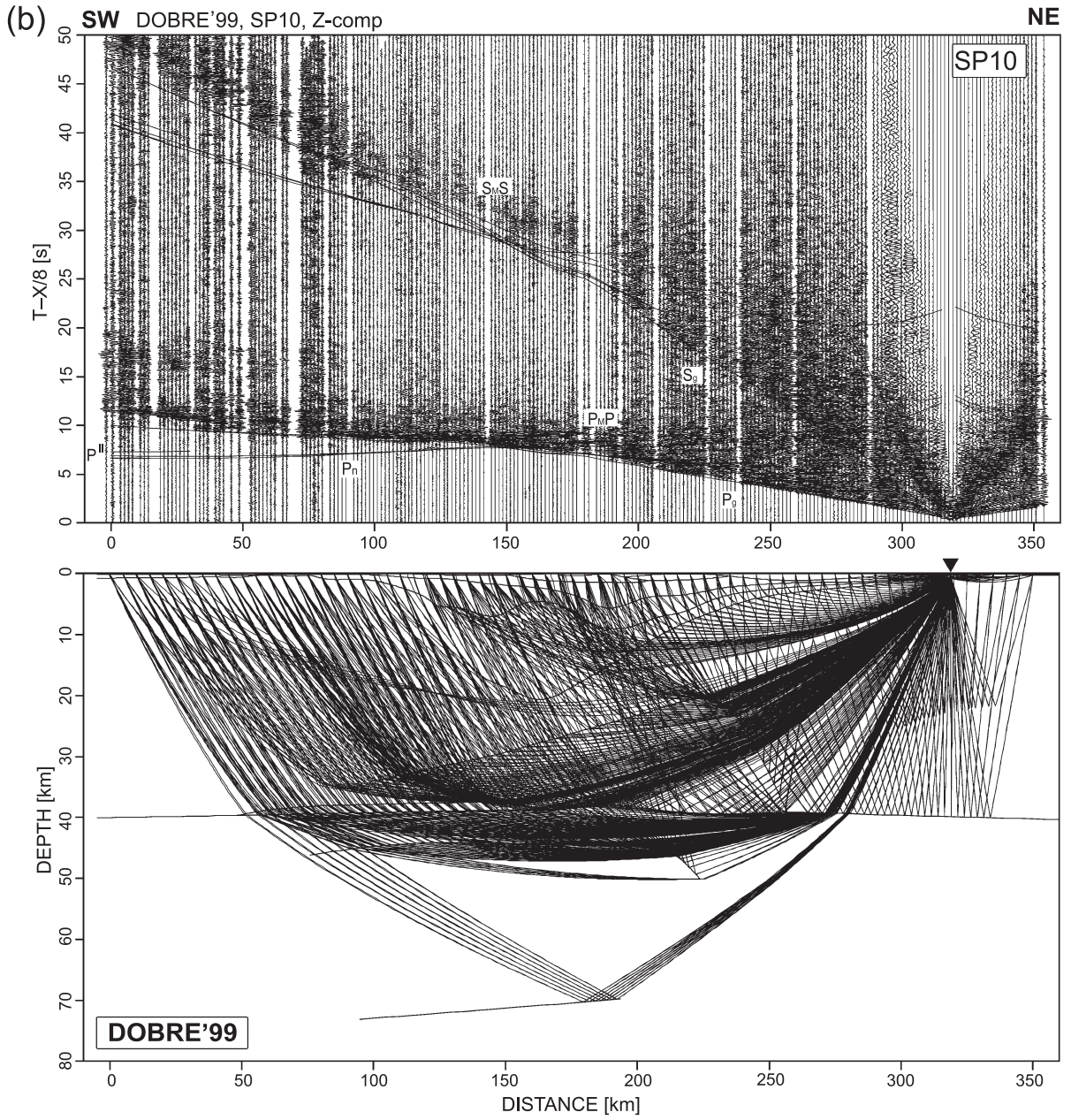

Fig. 10 (*continued*).

ry cover, head waves in the basement, diving waves in the lower crust, reflected waves from the Moho, diving waves in the upper mantle, and waves reflected from the discontinuities in the upper mantle. Travel time differences between observed and calculated phase arrivals in the final model are of the order of 0.1 s. This indicates a generally reliable result although it should be noted that for some deep reflections (e.g. from the Moho for SP01) no good coincidence was achieved.

The P-wave velocity model using the program SEIS83 (Červený and Pšencík, 1983), enhanced by interactive graphical interfaces MODEL (Kommi-naho, 1997) and ZPLOT (Zelt, 1992), is shown in Fig. 6c (Institute of Geophysics, Warsaw). Theoretical travel times, ray paths, and synthetic seismograms of refracted and reflected P- and S-phases were calculated and velocity distributions, depths of seismic boundaries in the crust and uppermost mantle, and the distribution of the Vp/Vs ratio in the crust were determined. The final P-velocity model (Fig. 6c) was found by trial-and-error. Model travel times were recalculated many times until close agreement (of the order 0.1 s) was obtained with the observed travel times. Examples (SP01 and SP09) of calculated travel times, with respective ray paths, compared to the observed data is shown in Fig. 9a–d. Synthetic seismograms were used to estimate velocity gradients in layers and velocity contrasts at seismic boundaries.

The best branches of correlated S-wave travel times were used to estimate the distribution of the Vp/Vs ratio for the main supracrustal and crustal layers. Preliminary analysis of corresponding P- and S-wave travel times indicated a potentially large Vp/Vs ratio variation throughout the model (Fig. 10). Accordingly, the geometry of an initial S-wave velocity model was derived from the final P-wave velocity model (Fig. 6c) and was then iteratively modified until a good fit was achieved to the observed travel times of refracted or/and reflected S-waves. Representative Vp/Vs values are plotted in Fig. 11.

The final model (Fig. 6c) shows a sedimentary sequence with profoundly variable structure and thickness along the profile. The most significant feature is the sedimentary basin beneath the Donbas Foldbelt; it is ~ 110 km wide (km 110–220) and up to 20 km thick. The sedimentary cover of the Azov

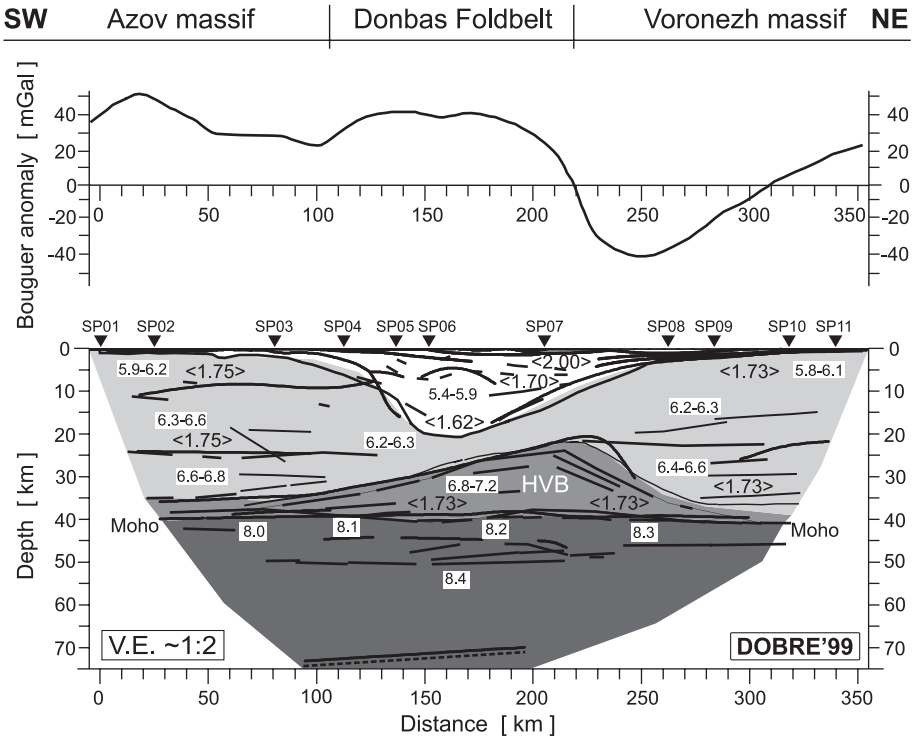

Fig. 11. Summary of the main attributes of the DOBREfraction'99 P-wave velocity models determined from ray-tracing methods. Velocities are in km s^{-1}; numbers in brackets ⟨⟩ are Vp/Vs ratios. Also shown is the variation of Bouguer gravity anomaly along the DOBREfraction'99 profile (top panel).

Massif to the southwest and Voronezh Massif to the northeast is relatively thin (up to ~ 3 km), which compares to what is well known from drilling and previous, detailed seismic studies. Velocities within the Donbas sedimentary succession are 4.2–5.4 km s^{-1} to a depth 8 km and 5.7–5.9 km s^{-1} to 20 km depth. The Vp/Vs ratio (cf. Fig. 11) changes from 2.00 near the surface to 1.70 at a depth of about 8 km to a markedly low value of 1.62 in the deepest part of the sedimentary basin.

The crystalline crust of the Azov and Voronezh massifs is about 35–40 km thick and displays a velocity increase from 5.9–6.1 km s^{-1} near the surfaced to ~ 6.8 km s^{-1} at depth. The velocity gradient is slightly smaller in the Voronezh Massif than in the Azov Massif. The crust in general has a rather transparent character with only few "floating reflectors" being inferred. Velocity contrasts at intracrustal boundaries are small, of the order 0.1 km s^{-1}. Velocities at the top of the Azov Massif basement are slightly less than for the Voronezh Massif (5.9–6.0 km s^{-1} compared to 6.1 km s^{-1}). Slightly higher Vp/Vs ratios are calculated for the Azov crust (1.75) compared to the Voronezh crust (1.73).

In the central part of the profile, beneath the Donbas Foldbelt, a lower crustal body with velocities $\geq$6.9 km s^{-1} is observed. Its presence is inferred from high velocity refracted and strong reflected waves (P_{HVB}, $P_{HVB}P$; e.g. Fig. 9a–d). The shape of the high velocity body (HVB) is asymmetric and the depth of its upper surface ranges from as little as ~ 20 km beneath the northern margin of the Donbas (at about 230 km along the profile) to about 35 km beneath Azov Massif. The calculated Vp/Vs ratio of the HVB is 1.73. The total thickness of the crust is approximately 40 km, with only small undulations along the profile, of the order $\pm$1 km.

The sub-Moho is 8.0 km s^{-1} beneath the Azov Massif and 8.3 km s^{-1} beneath the Voronezh Massif. A reflector is inferred in the uppermost mantle about 7 km beneath the Moho. In addition, a very deep lithospheric boundary (reflector) at ~ 70 km depth was inferred (cf. shot point SP08 (Fig. 3h) and SP10 (Fig. 10b)) in Fig. 11 but is not shown in Fig. 6. The reflector apparently dips slightly to the southwest.

5. Discussion

A compilation of the main features of the three P-wave velocity models shown in Fig. 6 is presented in Fig. 11, along with the Bouguer gravity anomaly variation along the DOBREfraction profile.

A well-defined sedimentary basin, with velocities from ~ 2.0–2.4 up to 5.8–5.9 km s^{-1}, is a feature of all models. Notable is the degree of resolution of intrabasinal structure afforded by the DOBREfraction data. Up to six distinct refraction layers were identified, though in detail these may not correspond directly with sedimentary layers. Although the velocity models resolve some indication of folding within the sedimentary succession, the actual wavelength of folding as seen in the surface geology of the DF is beyond the resolution of the refraction/wide-angle data.

The lowest velocities are confined to a layer of 2–3 km thickness on the northern margin of the DF, between shot points SP07 and SP10 (cf. Fig. 6). This corresponds to a Late Cretaceous sedimentary depocentre that may have formed as a response to inversion processes. There is also a direct correlation between the low velocity (Cretaceous) sedimentary layer and the gravity low that dominates the northern part of the gravity signature of the DF (Fig. 11). Given that the low velocity sedimentary layer lies at the surface and that the inferred density contrast of these sediments with adjacent Carboniferous sediments and basement rock is significant, it likely explains much of the gravity low. Preliminary gravity modelling, however, suggests that other factors, such as anomalous densities in the upper crust, may also be involved (Yegorova, personal communication, 2002).

The maximum thickness of the sedimentary basin is interpreted to be about 20 km, in keeping with previously made estimates based on the older DSS data cited earlier and with extrapolations from regional reflection-seismic profiles crossing the DDB northwest of the DF (Stovba and Stephenson, 1999). Such a depth to the top of crystalline basement is also in keeping with interpretations of the coincident DOBREflection deep seismic reflection profile (DOBREflection-2000 and DOBREfraction'99 Working Groups, 2002; Maystrenko et al., in press).

Significant variability of Vp/Vs ratio has been resolved for the basin fill. In particular, in the deepest part of the sedimentary fill of the Donbas Foldbelt, Vp/Vs ratio is significantly less than elsewhere in the basin (1.62 compared to 1.70 and 2.00 elsewhere). This is evidence for a significant bulk composition of salt and/or other evaporitic rocks in this part of the basin, since these kinds of materials typically have a rather low Poisson's ratio (e.g. Turcotte and Schubert, 1982). Though there has been some disagreement, conventional wisdom in recent years has been that there is no significant salt layer in the DF and hence no role for salt diapirism in its structural evolution (cf. Stovba and Stephenson, 1999). Elsewhere in the DDB, however, there is abundant evidence for the presence of salt rich bodies at great depth and that salt movements have been intimately involved in the formation of arches and domes during the Early Permian (e.g. Stovba et al., 1996; Stovba and Stephenson, in press). Thus, given the velocity evidence for the presence of a salt rich bulk composition at depth in the DF, it may be surmised that evidence for the existence of fold-like structures in the DF prior to maximum burial by the Early Permian (e.g. Sachsenhofer et al., 2002) could be related to halokinesis in a transtensional tectonic setting rather than to compressional tectonics. The very high Vp/Vs ratio inferred at shallow depths within the basin near its northern margin could be an indication of structural complexity, and concomitant complexity in seismic phase ray paths and correlations related to an imbricate zone of reverse faults (formed during to Late Cretaceous inversion).

The main crustal layer along the DOBREfraction profile, with velocities $\sim 5.8-6.8$ km s^{-1}, thins significantly beneath the main sedimentary depocentre. In turn, the higher velocity lower crustal (or crust–mantle mix) HVB layer, $\sim 6.9-7.2$ km s^{-1} thickens significantly in the same part of the profile. The shape of the sedimentary basin is asymmetric with the steepest crystalline basement surface on the southwestern margin of the basin. The shape of the HVB does not mirror the shape of the basin. It also displays an asymmetric shape but with its steepest upper surface beneath the northeastern margin of the basin. The HVB itself is readily interpreted as a zone of crustal underplating or "rift-pillow" (e.g. Ervin and McGinnis, 1975), commonly found in the lower crust beneath the axis of rift and other extensional sedimentary basins. As such, it is usually thought to comprise crustal material that has been intruded by mafic and/or ultramafic rocks during the rifting process. The asymmetry is evidence of some degree of so-called "simple-shear" rather than "pure-shear" during rifting (e.g. Buck et al., 1988), with the master detachment fault deepening in a listric manner from the southwestern basin margin to the top of the HVB layer. This has potential implications for the thermal evolution of the crust–basin system after rifting and, accordingly, for basin subsidence. No published subsidence model to date has taken into account any degree of simple-shear during rifting of the DDB.

The Moho depth is more or less constant along the entire profile (40 ± 2 km). In this respect, crustal thinning—taken as a whole—beneath the sedimentary basin is not particularly asymmetric. The maximum reduction of crustal thickness is about 50%, immediately beneath the deepest part of the basin. This is a slight underestimate given that the lower crustal layer has presumably incorporated (and been thickened by) mantle-derived magmas during the rifting process, at the same time as crustal thinning by extension occurred. A simple estimate, based on the observed velocity contrasts, is that a minimum of 10% but as much as 50% of the HVB comprises mantle material (e.g. Thybo et al., 2000). This implies an additional 2–9 km of crustal thinning during rifting and a maximum crustal "stretching factor" of as much as 2.25–2.5 (or more), a figure that compares favourably with what has been inferred from subsidence modelling in the vicinity of the DOBREfraction profile (Stovba et al., 2003).

According to studies of basement rocks on either side of the DDB, the regional structural grain and the boundaries of composite basement terranes lie perpendicular to the trend of the DDB rift (Shchipansky and Bogdanova, 1996). The basement structure, furthermore, does not display any obvious lateral offset across the rift zone. The style of faulting observed on seismic data within the DDB northwest of the DF also precludes significant strike-slip displacements within the rift zone (Stovba et al., 1996). However, the velocity model implies that there may be different crustal affinity on either side of the DF at the location of the DOBREfraction profile. Crustal velocities are slightly higher in the crust of the Azov Massif

(Ukrainian Shield) than of the Voronezh Massif, Vp/Vs ratios may also larger (1.75 versus 1.73, though this may not be statistically significant), whereas the velocity of the sub-Moho upper mantle is slightly less (8.0 compared to 8.3 km s^{-1}). The gravity profile also suggests a different crustal signature on either side of the rift zone.

However, it is also known that the southern margin of the DF was significantly uplifted since the time of rifting compared to the northern margin (during the Early Permian). Stovba and Stephenson (1999) suggested as much as 5–10 km uplift in the vicinity of the present southern rift margin. The mapped basement rocks of the Azov Massif display a higher grade of metamorphism and are thought be older than those to the north of the rift zone (Zaritsky, 1992). Sedimentary rocks of post-rift or even syn-rift affinity may have covered much of the currently exposed Azov Massif prior to uplift. Elevated velocities within the present-day Azov crust could therefore be related to this uplift (as originally more deeply buried levels were uplifted into their present positions). In turn, the reduced upper mantle velocity beneath the Azov Massif may be an effect or consequence of the mechanism that led to the uplift (which is otherwise poorly understood; cf. Stephenson et al., 2001; Saintot et al., in press). The asymmetric shape of the crystalline basement surface may have also been effected in part by the Early Permian uplift of the southern margin of the DF.

6. Summary and conclusions

The DOBREfraction'99 profile was the first deep seismic study designed to record upper mantle refracted phases from beneath the Donbas Foldbelt in Ukraine. Excellent data were recorded from 11 shots along a 360 km long profile and these constrain a velocity model of the crust (including overlying sedimentary layers) and upper mantle that indicate important modifications to previously held ideas. Among the significant features of crustal and upper mantle structure associated with the Donbas Foldbelt are the following:

1. The basement surface underlying the sedimentary rocks of the Donbas Foldbelt (Donets Basin) lies at a depth of about 20 km.
2. There is a considerable degree of resolution of velocity layers within the sedimentary basin; most sediments, being Devonian and Carboniferous syn- and post-rift sediments that have been deeply buried, display relatively high velocities (~ 5.0–5.9 km s^{-1}).
3. The youngest and lowest velocity (< 3 km s^{-1}) sedimentary layer (Cretaceous mapped at the surface) has a thickness of ~ 2 km; the Bouguer gravity low over the northern part of the Donbas Foldbelt correlates in position with the Cretaceous basin and can be in part attributed to it.
4. Modelled travel times of S-wave phases allow the inference of Vp/Vs ratios in some parts of the velocity model. In the Donbas Foldbelt the Vp/Vs ratio increases from ~ 2.0 near the surface to ~ 1.62 in the deepest part of the basin. There is a suggestion of a salt rich bulk composition for the lowermost part of the sedimentary basin (15–20 km depth), similar to what is observed in the uninverted part of the Dniepr–Donets Basin.
5. The shape of the sedimentary basin is asymmetric; the basement surface beneath the basin is steeper under the southwestern margin than under the northeastern margin.
6. A high velocity lower crustal layer (>6.9 km s^{-1}) thickens (up to 15–20 km thickness) beneath the Donbas Foldbelt; it has the form of a "rift pillow" forming as a result of lower crust being intruded by at least 10% mantle material during rifting.
7. The high velocity "rift pillow" has an asymmetric shape, more steeply bounded on its northeast margin than its southwest margin; together with the asymmetry displayed by the shape of the sedimentary basin, a component of simple-shear, detachment down to the northeast is suggested during rifting.
8. Crustal velocities are slightly higher to the southwest compared to the northwest of the sedimentary basin than the suggested corresponding density contrast appears to play a role in the shape of the gravity signature across the Donbas Foldbelt.
9. The level of the Moho is roughly constant (~ 40 km) across the Donbas Foldbelt, in contrast to previously published models, which did not include modelling of seismic phases refracted at the Moho and in the upper mantle.

10. Total crustal thinning across the Donbas Foldbelt (basement to Moho surfaces) is about one-half (stretching factor ~ 2), roughly consistent with subsidence modelling inferences, but this could be greater depending on the degree of fractionation of mantle material now residing in a lower crustal high velocity layer—or "rift pillow"—lying beneath the sedimentary basin.
11. A change in crustal affinity across the Donbas Foldbelt is not precluded although some of the observed differences across it could be consequences of Permian uplift more strongly affecting the southwestern rift margin than the northeastern margin.

Acknowledgements

The DOBRE project developed within the framework of the European Science Foundation EUROPROBE Programme. The National Academy of Sciences of Ukraine (via the Institute of Geophysics, Kyiv) and the Ukrainian Ministry of Ecology and Natural resources (via Ukrgeofisika) provided financial and management support during fieldwork and follow-up operations. The Polish Academy of Sciences paid the fieldwork expenses of Polish participants. Remaining DOBREfraction'99 operational costs were paid by the Netherlands Centre for Integrated Solid Earth Sciences (ISES). Personnel employed by the University of Copenhagen, Denmark, and the University of Texas at El Paso participated in the fieldwork. Timing equipment for shots was provided by Polish Oil and Gas and Geophysical Enterprise in Toruń, Poland. In the US, IRIS/PASSCAL supports the instrument pool that made the DOBREfraction'99 fieldwork possible. These instruments were developed and purchased with a grant from the Texas Higher Education Co-ordinating Board. The Texans provided by the University of Copenhagen were donated by the Carlsberg Foundation (Copenhagen). The University of Copenhagen also received support from the Danish Natural Sciences Research Council (SNF). Many activities ancillary to DOBRE were carried out as part of INTAS project 97-0743; some directly related expenses incurred by the Institute of Geophysics, Kyiv, were paid by INTAS. A. Andrievsky of Ukrgeofisika proposed the name DOBRE as an acronym for Donbas Refraction and Reflection. The following persons are also thanked for essential contributions and/or support during the years that the DOBRE project matured: S. Cloetingh, D. Gee, S. Goshovsky, and S. Lizun. Many other individuals, too numerous to be mentioned here, contributed to the success of the field surveys. A special mention is made to the observers and technical experts who participated in the fieldwork and data processing. Finally, the authors thank an anonymous Tectonophysics reviewer and N. Pavlenkova for their comments, which have led to an improved revised manuscript.

References

Borodulin, M.I., 1978. Some problems of the evolution of the Earth's crust of the Donets basin. Geoph. Sb. Ukr. SSR 82, 61–66 (in Russian).

Borodulin, M.I., Khokhlov, M.T., 1970a. On a method of seismic studies and some results of studying the basement in the Donets basin. Rep. Ac. Sci. Ukr. SSR, Ser. B6, 506–509 (in Russian).

Borodulin, M.I., Khokhlov, M.T., 1970b. Features of the method of studying the velocity characteristics of the sedimentary mass of Donbas. Rep. Ac. Sci. Ukr. SSR, Ser. B7, 591–595 (in Russian).

Borodulin, M.I., Mikhalev, A.K., 1973. New data on deep structure of Western Donbas. Rep. Ac. Sci. Ukr. SSR, Ser. B6, 651–655 (in Russian).

Buck, W.R., Martinez, F., Steckler, M.S., Cochran, J.R., 1988. Thermal consequences of lithospheric extension: pure and simple. Tectonics 7, 213–234.

Červený, V., Pšencík, I., 1983. SEIS83-numerical modeling of seismic wave fields in 2-D laterally varying layered structure by the ray method. In: Engdahl, E.R. (Ed.), Documentation of Earthquake Algorithm. World Data Center A for Solid Earth Geophysics, Boulder, Rep. SE, vol. 35, pp. 36–40.

Chekunov, A.V., Gavrish, V.K., Kutas, R.I., Ryabchun, L.I., 1992. Dnieper–Donets paleorift. In: Ziegler, P.A. (Ed.), Geodynamics of Rifting, vol. I. Case History Studies on Rifts: Europe and Asia. Tectonophysics, vol. 208, pp. 257–272.

DOBREflection-2000 and DOBREfraction'99 Working Groups, 2002. DOBRE studies evolution of inverted intracratonic rifts in Ukraine. Eos, 83, 323, 326–327.

Ervin, C.P., McGinnis, L.D., 1975. Reelfoot rift: reactivated precursor to the Mississippi Embayment. Geol. Soc. Amer. Bull. 86, 1287–1295.

Garkalenko, I.A., Borodulin, M.I., 1972. Deep tectonics of the Donets basin. Geoph. Sb. Ukr. SSR 48, 80–89 (in Russian).

Garkalenko, I.A., et al., 1970. Results of deep seismic soundings along the profiles Nogaisk-Konstantinovka-Svatove (Western Donbas). Geoph. Sb. Ukr. SSR 37, 15–23 (in Russian).

Gee, D.G., Zeyen, H.J. (Eds.), 1996. EUROPROBE 1996—Lithosphere Dynamics: Origin and Evolution of Continents. EUROPROBE Secretariat, Uppsala University. 138 pp.

Hole, J.A., 1992. Non-linear high-resolution three-dimensional seismic travel-time tomography. J. Geophys. Res. 97, 6553–6562.

Ilchenko, T.V., 1992. Seismic model of the Earth's crust along the DSS-profile Near-Azov Massif–Donbas–Voronezs Massif. Geophys. J. (Kyiv) 14 (5), 50–59 (in Russian).

Ilchenko, T., 1996. The Dniepr–Donets Rift: deep structure and evolution from DSS profiling. Tectonophysics 268, 83–98.

Ilchenko, T.V., Stepanenko, V.M., 1998. A velocity model of the Earth's crust and upper mantle of Donbas and its geological interpretation. Geophys. J. (Kyiv) 20 (2), 95–105 (in Russian).

Komminaho, K., 1997. Software manual for programs MODEL and XRAYS—a graphical interface for SEIS83 program package. University of Oulu, Department of Geophysics, Rep. No. 20. 31 pp.

Kusznir, N.J., Kovkhuto, A., Stephenson, R.A., 1996a. Syn-rift evolution of the Pripyat Trough: constraints from structural and stratigraphic modelling. Tectonophysics 268, 221–236.

Kusznir, N.J., Stovba, S.M., Stephenson, R.A., Poplavskii, K., 1996b. The formation of the northwestern Dniepr–Donets Basin: 2-D forward and reverse syn-rift and post-rift modelling. Tectonophysics 268, 237–255.

Maystrenko, Yu., Stovba, S., Stephenson, R., Bayer, U., Menyoli, E., Gajewski, D., Huebscher, C., Rabbel, W., Saintot, A., Starostenko, V., Thybo, H., Tolkunov, A., 2003. Crustal-scale pop-up structure in cratonic lithosphere: DOBRE deep seismic reflection study of the Donbas Foldbelt, Ukraine. Geology (in press).

Nikishin, A.M., Ziegler, P.A., Stephenson, R.A., Cloetingh, S.A.P.L., Furne, A.V., Fokin, P.A., Ershov, A.V., Bolotov, S.N., Korotaev, M.V., Alekseev, A.S., Gorbachev, V.I., Shipilov, E.V., Lankreijer, A., Bembinova, E.Yu., Shalimov, I.V., 1996. Late Precambrian to Triassic history of the East-European craton: dynamics of sedimentary basin evolution. Tectonophysics 268, 23–63.

Pavlenkova, N.I., 1995. Double Moho in the Dnieper–Donets basin. Comptes Rendues de l'Academie des Sciences de Paris, t. 321, série Iia, 85–93.

Sachsenhofer, R.F., Privalov, V.A., Zhykalyak, M.V., Bueker, C., Panova, E.A., Rainer, T., Shymanovskyy, V.A., Stephenson, R., 2002. The Donets Basin (Ukraine/Russia): coalification and thermal history. Int. J. Coal Geol. 49, 33–55.

Saintot, A.N., Stephenson, R.A., Brem, A., Stovba, S., Privalov, V., 2003. Paleostress field reconstruction and revised tectonic history of the Donbas fold-and-thrust belt (Ukraine and Russia). Tectonics (in press).

Shchipansky, A., Bogdanova, S., 1996. The Sarmatian crustal segment: Precambrian correlation between the Voronezh Massif and the Ukrainian Shield across the Dniepr–Donets Aulacogen. Tectonophysics 268, 109–126.

Sollogub, V.B., Borodulin, M.I., Chekunov, A.V., 1977. Deep structure of Donbas and adjacent territories. Geophys. J. 37 (2), 23–31 (in Russian).

Stephenson, R.A., EUROPROBE Intraplate Tectonics and Basin Dynamics Working Group, 1993. Continental rift development in Precambrian and Phanerozoic Europe: EUROPROBE and the Dnieper–Donets rift and Polish Trough basins. Sediment. Geol. 86, 159–175.

Stephenson, R.A., Stovba, S.M., Starostenko, V.I., 2001. Pripyat–Dniepr–Donets Basin: implications for rift geodynamics and northern Peri-Tethyan tectonic history. In: Ziegler, P.A., Cavazza, W., Robertson, A.H.F. (Eds.), Peri-Tethyan Rift/Wrench Basins and Passive Margins, Peri-Tethys Memoir 6. Mémoires du Muséum National d'Histoire Naturelle, vol. 186, pp. 369–406.

Stovba, S.M., Stephenson, R.A., 1999. The Donbas Foldbelt: its relationships with the uninverted Donets segment of the Dniepr–Donets Basin, Ukraine. Tectonophysics 313, 59–83.

Stovba, S.M., Stephenson, R.A., 2003. Style and timing of salt tectonics in the Dniepr–Donets Basin (Ukraine): implications for triggering and driving mechanisms of salt movement in sedimentary basins. Mar. Pet. Geol. (in press).

Stovba, S.M., Stephenson, R.A., Kivshik, M., 1996. Structural features and evolution of the Dniepr–Donets Basin, Ukraine, from regional seismic reflection profiles. Tectonophysics 268, 127–147.

Stovba, S.M., Maystrenko, Yu.P., Stephenson, R.A., Kusznir, N.J., 2003. The formation of the south-eastern part of the Dniepr–Donets Basin: 2-D forward and reverse syn-rift and post-rift modelling. Sediment. Geol. 156, 11–33.

Thybo, H., Luetgert, J., 1990. RAY84PC—Two-dimensional Ray-tracing and Synthetic Seismogram Calculation on Personal Computers. Institute of Geology, Copenhagen. 41 pp.

Thybo, H., Maguire, P., Birt, C., Perchuc̀, E., 2000. Seismic reflectivity of the lower crust and magmatic underplating beneath the Kenya Rift. Geophys. Res. Lett. 27, 2745–2749.

Turcotte, D.L., Schubert, G., 1982. Geodynamics: Applications of Continuum Physics to Geological Problems. Wiley, New York. 449 pp.

Vidale, J.E., 1990. Finite-difference calculation of travel-times in three dimensions. Geophysics 55, 521–526.

Wilson, B.M., Lyashkevich, Z.M., 1996. Magmatism and the geodynamics of rifting of the Pripyat–Dnieper–Donets rift, East European Platform. Tectonophysics 268, 65–81.

Zaritsky, A.I., 1992. Geology and metallogeny of the south-western part of the East-European Platform: Ukrainian Shield, Voronezh and Belarussian massifs. Scale 1:1.000.000. Geological Committee of Ukraine, Kyiv.

Zelt, C.A., 1992. Seismic program package ZPLOT. Personal communication.

Zelt, C.A., 1999. Modelling strategies and model assessment for wide-angle seismic travel-time data. Geophys. J. Int. 139, 183–204.

Zelt, C.A., Smith, R.B., 1992. Seismic travel-time inversion for 2-D crustal velocity structure. Geophys. J. Int. 108, 16–34.

Zonenshain, L.P., Kuzmin, M.I., Natapov, L.M., 1990. Geology of the USSR: a plate tectonics synthesis. In: Page, B.M. (Ed.), Geophysics Geodynamics Series, vol. 21. American Geophysical Union, Washington, DC. 242 pp.